Novel oxides with interesting ionic, electronic and/or magnetic properties.

A dissertation submitted for the degree of

Philosophiæ Doctor (PhD)

By:

Laurent Jantsky

Department of Chemistry,

Faculty of Mathematics and Natural Science,

University of Oslo.

February - 2012

© Laurent Jantsky, 2012

Series of dissertations submitted to the
Faculty of Mathematics and Natural Sciences, University of Oslo
No. 1183

ISSN 1501-7710

All rights reserved. No part of this publication may be
reproduced or transmitted, in any form or by any means, without permission.

Cover: Inger Sandved Anfinsen.
Printed in Norway: AIT Oslo AS.

Produced in co-operation with Unipub.
The thesis is produced by Unipub merely in connection with the
thesis defence. Kindly direct all inquiries regarding the thesis to the copyright
holder or the unit which grants the doctorate.

Abstract.

This work summarises the outcome of research performed at the Universities of Liverpool and Oslo during the course of an EU-Marie Curie EST fellowship and funded through the NOVELOX program under the 6th framework (FP6) of the European Union. It focuses on perovskite related materials that possess the Ruddlesden-Popper structure and are composed of Pr-Sr-Co-Fe-O atoms.

After an introduction chapter that aims at presenting a general overview of perovskites and related materials through their structures and technological applications, a brief description of the experimental methods used throughout this work is given in Chapter 2. The third chapter summarises non published but relevant results as well as summaries of published, submitted or under review manuscripts. It begins by describing the attempts at lanthanide substitution within the $LnSr_3Co_{1.5}Fe_{1.5}O_{10-\delta}$ system and the subsequent choice of Ln=Pr. It is then followed by an account of the effect of oxygen deficiencies in $PrSr_3Co_{1.5}Fe_{1.5}O_{10-\delta}$ on the oxidation state of the transition metals and their local magnetic environment and behaviour as examined respectively by XANES and Mössbauer spectroscopy. These confirm the reduced state of the transition metal cations as well as the presence of magnetic ordering. Thereafter results summarising the structural evolution of the compound upon heating under inert conditions (Paper I) and the subsequent hydration of the thus obtained phases (Paper II) are given. It is shown that the onset of oxygen mobility occurs at relatively low temperatures (c.a. 200°C) and a conduction mechanism is proposed. For the reduced phases, hydration as well as carbonation is shown to occur as a function of the hydration mechanism used. In addition, the topotactic de-hydration through a hydroxide phase, as studied by in-situ synchrotron radiation experiments, is also discussed. The chapter terminates by summarizing the impact of Co for Fe substitution on the magnetic properties and structure of $PrSr_3Co(Fe_{1-x}Co_x)_3O_{10-\delta}$ (x=0.0 to 0.6, Paper III). As the Co content increases, the transition from a complex anti-ferromagnetic structure, to one where ferromagnetic interactions are dominant is observed.

Finally, a discussion on the possibilities that this work offers followed by the list of publications and references terminate this thesis. Complete reproductions of the publications are to be found in the Annexe of this work.

Acknowledgments.

After 5 years university study, choosing to proceed with a PhD proved a definite choice of lifestyle. With its ups and downs, setbacks and leaps it required a bit of luck, some clever ideas, a fair dose of perseverance, lots of support... and of course an interesting research topic. The latter was provided courtesy of the Marie-Curie Research network, through an Early Stage Training fellowship (MEST-CT-2004-514237) that was coordinated by Prof B. Raveau (CRISMAT – Caen) with Prof M.J. Rosseinsky (University of Liverpool) and Prof. H. Fjellvåg (University of Oslo) as collaborators.

For giving me the opportunity to work on this project and providing supervision whilst in Liverpool, I wish to thank in particular Prof M.J Rosseinsky. I am also indebted to my supervisor, Prof H. Fjellvåg whom I wish to thank for his guidance, patience, trust as well as for doing his utmost to ensure the successful outcome of this work.

For their help, the fruitful discussions around tea/coffee/beers, the biscuits, the beamtimes, the skiing, their friendship and so much more, many many thanks go to: Barbara, John, Andrew, Matthew S, Xiaojun, Helen, Chris, Carlos, Calum, Mathieu, Hiroshi, Fede, Hops, Katarina, Rune, Karina, Pascal, Mehdi, Mari, Heidi, Erik, Mona, Dave, Mad, Yael, Aga, Jon, Ola, Per, Marc, Matthias, Frederic, Antoine, Demi, Nina, Poul, Truls, Reidar, Harald and all the other fantastic people that I was lucky to meet in Liverpool, Oslo, at beamlines and conferences.

However, most of all, I wish to thank my family and my wife for putting up with me, encouraging me and always believing that I could make it to the end of the PhD even when I started to doubt myself.

Finally, I wish to dedicate this work to those that are dear to me but not here any longer: Nagyapó, Mamicka, Grand-maman and Grand-papa.

Table of Contents

Table of Figures

Glossary

Structures:

a_p: The reduced dimension of a primitive perovskite cubic cell. (used to compare and represent derived super cells)

c_p: The reduced dimension of an anisotropic primitive perovskite cubic cell. (used to compare and represent derived super cells)

RPn: Ruddlesden Popper phase with "n" perovskite blocks alternating with on AO layer.

MIEC.: Mixed ionic and electronic conductor.

HTSC: High Temperature Super Conductor.

Properties:

JT: Jahn-Teller.

CD: Charge Disproportionation.

CO: Charge Ordering.

MI: Metal insulator transition.

PM: Paramagnetic.

(A)FM: (Anti-) Ferromagnetic.

FiM: Ferrimagnetic.

SG: Spin glass.

(A)FE.: (Anti-)Ferroelectric.

PE: Paraelectric.

MR (G-, T-or C-): Magneto resistance (Giant-, Tunnelling- or Colossal-)

Methods:

RT: Room temperature

ED: Electron diffraction

XRD (HR-, SR-): X-ray Powder diffraction (High Resolution-, Synchrotron Radiation-)

NPD: Neutron Powder Diffraction

EDS: Energy Dispersive X-ray Spectroscopy

EXAFS: Extended X-Ray absorption Fine Structure

XANES: X-ray Absorption Near Edge Spectroscopy

1 Introduction

Amongst the plethora of inorganic structures, there is one that stands out through its versatility in derived structures and physical properties: the perovskite structure.

"Perovskite" is a naturally occurring mineral with composition $CaTiO_3$ (with regional variations) that was named in honour of the Russian mineralogist Count Lev Alekseevich Perovskii by G. Rose in 1839.[1] Since then, other minerals and synthetic compounds of general composition ABX_3 that adopt a structure akin to $CaTiO_3$ have been referred to as perovskites. Generally, A and B are cations from group I through group XV elements and X is a counter anion from Group XV, Group XVI or Group XVII.

Along with their related structures, perovskites have been widely studied for their interesting properties since the mid 1940's[2] and have found many applications within an abundance of fields. These range from the "high-k" dielectrics (eg. Ba-$SrTiO_3$[3-5]), multiferroïcs (eg, $BiFeO_3$[6]), superconductors ($YBa_2Cu_3O_7$, La_2CuO_4), metallic conductors ($(La_{1-x},Sr_x)CoO_3$), magnetoresitors (MR) as exemplified by $LaMnO_3$, complex ferro- (FM) and antiferro- (AFM) magnetic structures all the way to high temperature catalysts and membrane materials.

This first chapter aims at presenting a general overview of perovskites and related materials through their structures and technological applications thereby setting the stage for the scope of this work. For the interested reader, a more in depth review on the relations between the perovskite structure and those of its related materials has been written by Mitchell.[7]

1.1 The ABX_3 Perovskites.

The wide range of applications where perovskites (and related) materials are to be found, is largely due to the compositional versatility of the structure. This allows for tuning of properties and stability by (co-) substitution and creation of ordered super-, defect- and intercalated structures.

The ideal perovskite structure is cubic and can be exemplified by that of $SrFeO_3$. In this structure, Sr is located on the A-site situated in the centre of the unit cell (i.e. x, y, z = ½, ½, ½), Fe is located on the B-site at one of the corners (i.e. x, y, z = 0, 0, 0) and the anion X-site is located halfway between two B-sites on a unit cell edge (i.e. x,y,z = ½, 0, 0) (Fig 1a lower sructure). It is a closed packed structure formed by the AX sublattice with the B cation occupying ¼ of the octahedral sites. The upper structure in Fig 1 (a) gives an alternative representation through a translation of the original unit cell by a vector (½, ½, ½).

However, only a few compounds possess an ideal cubic structure. Already in 1946, Megaw and co-workers published a comprehensive review of the then known perovskite structures[2] comprising cubic and distorted compounds. Using the available crystallographic data for the known perovskite structures, Goldschmidt proposed a tool for assessing and predicting the likely distortions. Based on geometric considerations of the ionic radii alone, he introduced the tolerance factor "t"[8].

$$t = \frac{R_A + R_X}{\sqrt{2}.(R_B + R_X)} \qquad (1)$$

Where R_A, R_B and R_X are respectively the ionic radii of cations on the A, B and X sites.

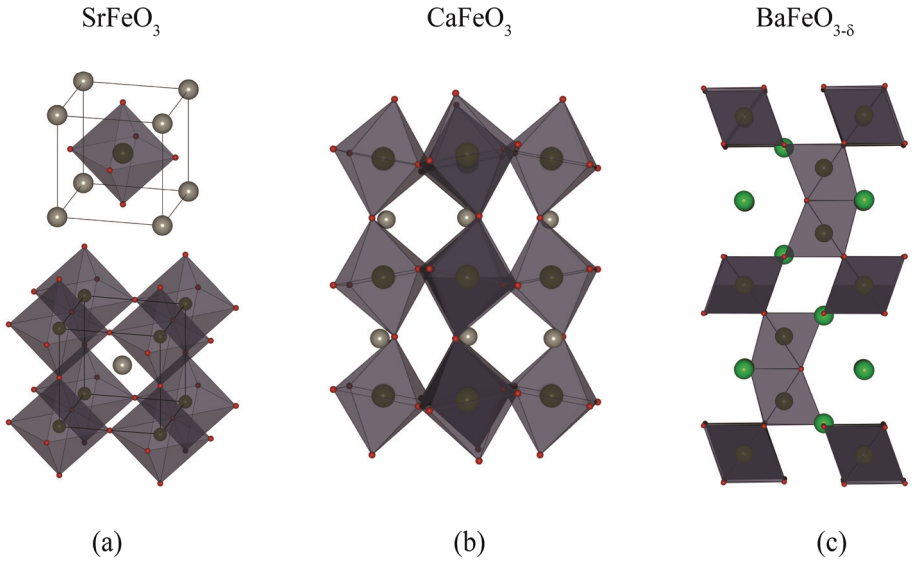

Fig 1. The different perovskite structures obtained when t≈1, t<1 or t>1. (a) 2 possible representations for the cubic $SrFeO_3$[9] with the BO_6 octahedra in the centre of the unit cell (top) or on the corners of the unit cell (bottom). (b) The orthorhombic $CaFeO_3$.[10, 11] (c) The hexagonal structure of $BaFeO_{3-\delta}$.[12]

The case of the $AFeO_3$ perovskites (A= Ca, Sr, Ba) provides an ideal illustration of these size effects. When "t" is much smaller than 1 as in $CaFeO_{3-\delta}$ (Fig 1b), the B-X bonds are put under a compressive strain causing the octahedral to tilt, thereby adopting an orthorhombic structure type. Glazer[13] has determined a series of notations to characterise these rotations and linked them to various crystallographic space groups.

When "t" is much greater than 1, as seen with $BaFeO_{3-\delta}$ (Fig 1c), the B-X bonds are put under tension resulting in hexagonal/rhombohedral structures with alternating sequences of hexagonal- and cubic- closed packing (hcp and ccp respectively) of the AX lattice.

Such deformations have a major effect on the properties of perovskites. As an example one might consider the $AFeO_3$ compounds (A= Ca, Sr, Ba). For these, the "s" atomic orbitals of the A cations lie too far from the Fermi level to have a major influence on the electronic properties of the compounds. These are therefore mainly governed by the cation on the B site (i.e.: Fe) and the B-O interactions. The orbital overlap between the 3d shell of Fe^{4+} and the 2p shell of the O^{2-} shells changes significantly when considering A=Sr^{2+} or A=Ca^{2+}. In the cubic $SrFeO_3$, the Fe^{4+} and O^{2-} are collinear allowing for maximum overlap of the Fe e_g orbitals and the O^{2-}p orbital thus creating a delocalised band. The width W_σ of this band can be related to the departure of the bond angle $\widehat{\text{Fe-O-Fe}}$ from 180° i.e. "180°-Φ" according to (2).[14]

$$W_\sigma \approx C.\,2\cos(\Phi) \qquad (2)$$

Where, C is a collection of terms reflecting the inter- and intra- atomic spin-spin interactions.

Upon substitution of Sr^{2+} by Ca^{2+}, the structure is distorted, the Fe-O-Fe angle is no longer 180° and the band width of the delocalised electrons diminishes. The compound goes from being a metallic compound to a semiconductor. When substituted by Ba^{2+}, the hexagonal form leads to strong deviations of the M-O-M angles from the ideal 180° resulting in a smaller bandwidth W_σ. However, the hexagonal distortion also leads to face sharing octahedra thus to smaller B-B distances. The electronic interactions between the B sites can therefore no longer be excluded and a more complex description is needed to explain the electronic properties of the compound.

In addition to the structural deformations caused by A-B size effects, magnetic interactions through super exchange and double exchange, Jahn-Teller (JT) deformations and charge disproportionation (CD) with charge ordering (CO), all of which may have an effect on the spin alignments of magnetic cations as well as cation ordering in substituted compounds, can lead to the emergence of super cells that enlarge the basic unit cell of the compound.

Fig 2 shows two examples of A site cationic ordering schemes. Both types are driven by the size differences between the A and A' cations. In the first case (Fig 2a), $AA'_3TM_3O_{12}$ (A is a La[15],Ca[16], A' is Mn[17] or Cu[15, 16] and TM a transition metal[15-17]) there is a 1:3 ordering between the A and A' cations accompanied by a cooperative tilting of the octahedra so as to

allow a square planar coordination between the A' and the oxygens. This has the effect of

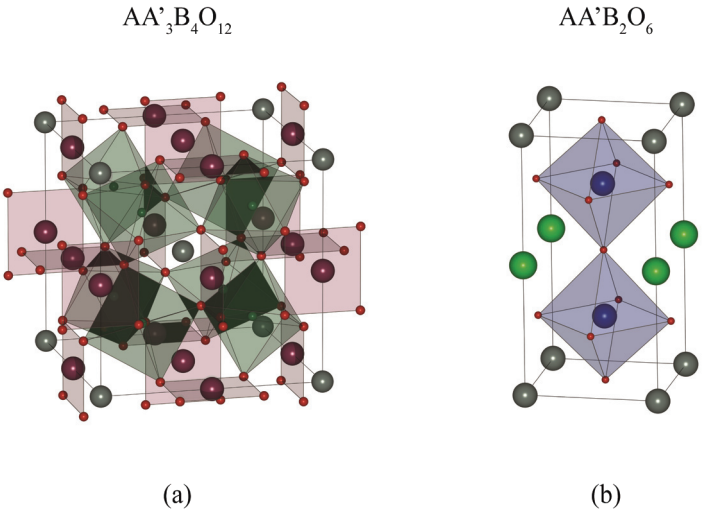

Fig 2. Perovskite structures with A site ordering. (a) A perovskite with a cationic 1:3 ordering ratio between two different cations (A' in purple and A grey) present on the A site.[15] (b) A perovskite with a 1:1 ordering ratio between the two cationic species present on the A site (green and grey atoms[18, 19]).

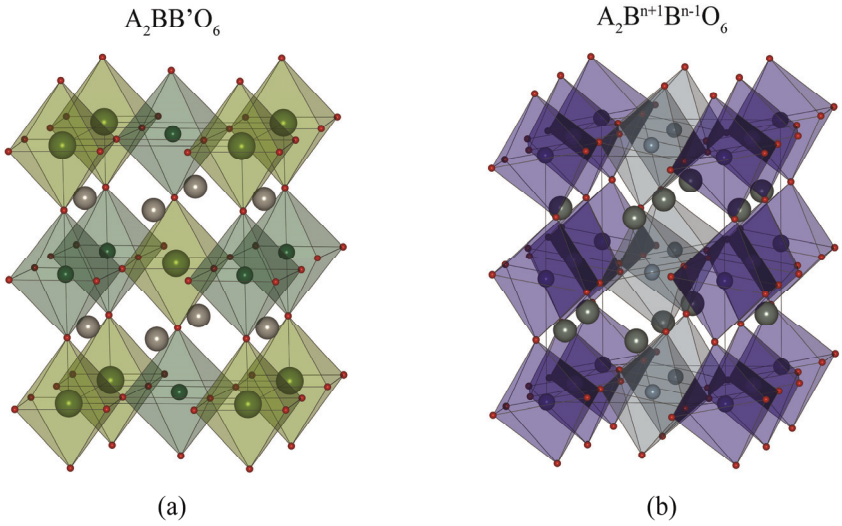

Fig 3. Perovskite structures with B site ordering. (a) A perovskite with a cationic 1:1 ordering ratio between two different cations present.[20] (b) Model for a perovskite with CO.[21]

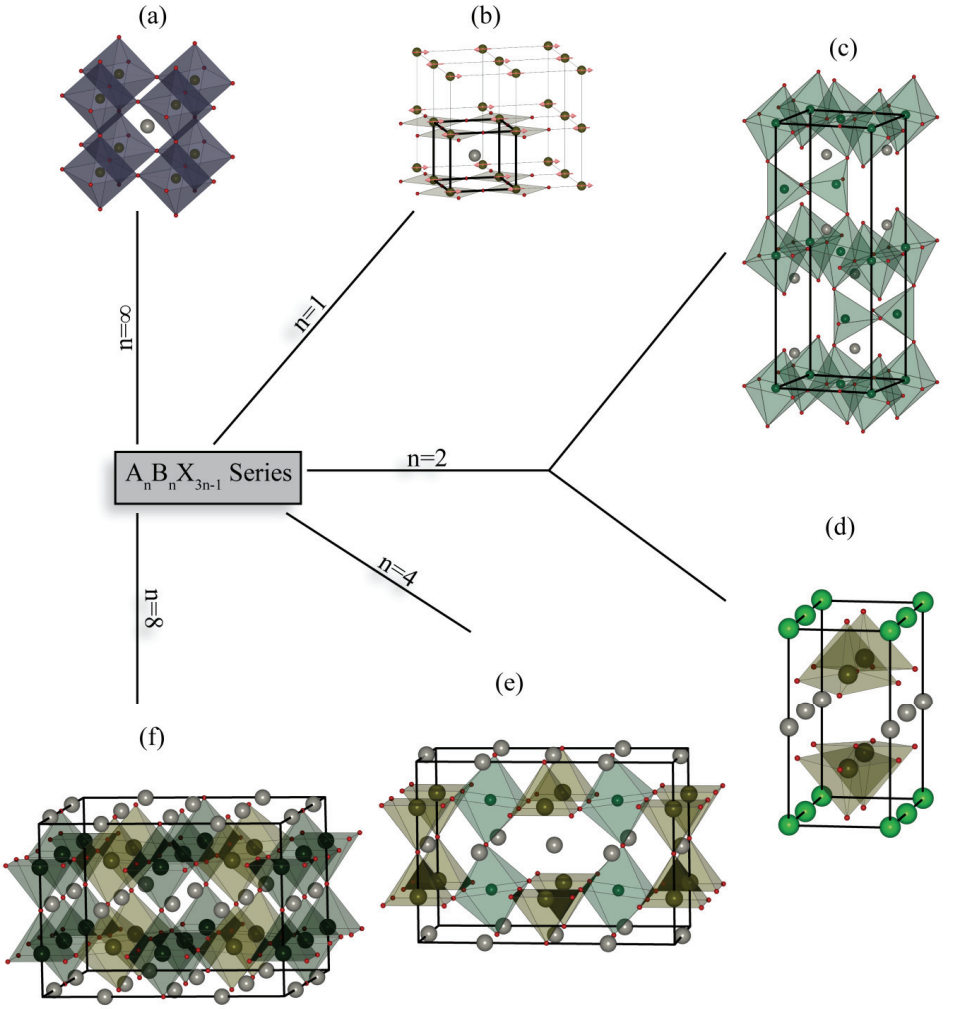

Fig 4. Ordered anion defect perovskite structures from the $A_nB_nX_{3n-1}$ system. (a) n=∞ The cubic perovskite.[9] (b) The n=1 member with its extended magnetic unit cell.[22] (c) The n=2 brownmillerite-type structure.[23] (d) The structure of $NdBaFe_2O_5$ at low temperatures, an alternative structure model for n=2[24-26] and structures for the n=4 (e) and n=8 (f) members.[23]

doubling the unit cell in all directions (**a** x **b** x **c** =$2a_p$ x $2a_p$ x $2a_p$). In the second scheme (Fig 2 b), the A' and A order in separate planes[18, 19, 27] resulting in a doubling of the unit cell along the c-axis (**a** x **b** x **c** =a_p x a_p x $2a_p$).

Similarly to what happens for the A site, B site order following substitution is encountered frequently in the ABX_3 systems. Though, in this case rather than being driven by size mismatches, it is rather charge mismatches or CD effects that drive such ordering. Figure 3 depicts these two situations. In part (a), an $A_2BB'O_6$ double perovskite structure is represented. Such ordering is typical of structures where 3d and 4d transition metals are mixed in a 1:1 ratio. Amongst the B cations that undergo charge CD/CO, those containing Mn^{3+}/Mn^{4+} or $Fe^{3+}/Fe^{4+}/Fe^{5+}$ compose one of the more commonly encountered groups. Fig 3(b) shows the case of a CO structure proposed for $La_{0.5}Ca_{0.5}MnO_3$ where the Mn^{3+} and Mn^{4+} are ordered in separate layers.

Other ordering schemes can be found for oxidation sates of the transition metals as in $Sr_2LaFe_3O_9$[28], where there is a 2:1 charge ordering of the Fe^{3+} and Fe^{5+}. These are often accompanied by orbital ordering and/or electron holes ordering that add to the variety of the superstructures found in these compounds.

1.2 Anion defective perovskite structures.

Many of the cations that can be accommodated by the perovskite structure have multiple stable valences. Therefore, the occurrence of anion vacancies in structures with cations in their lower oxidation states should not be unexpected. On the contrary, since the AX lattice forms a closed packed structure, the occurrence of interstitial anions is not likely, and it has been shown for hypostoichiometric $LaMnO_{3+\delta}$, that the structure comprises cationic vacancies and is more accurately described when written as $La_{1-x}\square_xMn_{1-y}\square_yO_3$[29]. Such cation deficient phases are treated in section 1.3.

Most probably one of the more obvious anion defective structures is that of the perovskite itself $ABX_{3-\delta}$. The vacancies are then distributed randomly over the available sites and the retained structure is often the same as the oxidised parent compound (Fig 4 a).

There are however some structure types that are more stable for specific values of δ. A large group of these has been regrouped under the generic formula $A_nB_nX_{3n-1}$. In this formula, "n" takes integer values, and for n=∞, the original oxidised perovskite is found. The cations on the A and B sites have a big influence on the values that n can take due to preferred coordination

environments and/or valences. This can be seen notably through the difference in structures adopted for the defective manganates and ferrates.

The $A_nFe_nO_{3n-1}$ series where n=1, 2, 4, 8 and ∞ is represented in Fig. 4 and correspond to "δ" values of 1, 0.5, 0.25, 0.125 and 0 respectively. The n=1 compound was synthesised by Tsujimoto and co-workers[22] in 2007 through the reaction of $SrFeO_3$ with CaH_2. As can be seen from Fig 4b, it consists of infinite planes of square planar $[FeO_2]^{2-}$ sheets separated by Sr^{2+} cations. This leads to a structural anisotropy reflected by the unit cell dimensions where a = b ≠ c. The compound has an AFM alignment of the Fe(II) spins within the sheets and aligned parallel to one of the crystallographic axis that leads to a magnetic super-cell doubled in all directions ($2a_p$ x $2a_p$ x $2c_p$). The transformation from the n=∞ to the n=1 phase is reversible and occurs through a n = 2 Brownmillerite-type intermediate.[22] This phase is shown in Fig 4c where A=Ca^{2+} and consists of corner sharing octahedraly (i.e. six-) coordinated Fe^{3+} sheets. The sheets of octahedra are separated by chains of corner shared Fe^{3+} tetrahedra. Fig 4d represents an alternate configuration for the n=2 member where the Fe is now five coordinated in a square pyramidal configuration.[24-26] In this case, such a configuration might be preferred due to the simultaneous ordering of Ba^{2+} and Nd^{3+} on the A-site. As can be seen from Fig 4e and Fig 4f, the higher order members consist of various ordering schemes of the octahedral and square pyramidal environments. For n=4, the five coordinated iron cations form sheets that are separated by sheets of octahedra whereas the n=8 consist of corner sharing Fe bi-pyramids that are stacked along one crystallographic axis. The stacks are surrounded by six chains of corner sharing octahedra. Furthermore, by co substitutions on the A and/or B site, ordered structures for n=3 have been found in a ccp derived AX arrays.[30] Compositions corresponding to n=3, 5, 6, 7, 10, 12 are also reported for various Fe-based rhombohedral and hexagonal perovskite systems resulting in various stacking sequences within the hcp - AX array[12, 31, 32] and are usually classified amongst hexagonal perovskite polytypes.

A final comment on the anion deficient compounds, the presence of ordered anion defects and cation ordering can occur simultaneously. Such phases typically occur with the cuprates and have as its most notorious example the "123" compound $YBa_2Cu_3O_7$ system (see Fig 8 (c)).

1.3 Perovskite related phases.

In addition to the compositional versatility of the perovskite $ABX_{3-\delta}$ (super-) structures, there exists a smorgasbord of structures that are related to it. That range from intergrowth of

perovskite and (un-) related phases through to anti-perovskites and hybrid Organic/Inorganic perovskites. An attempt to systematically classify all of them is out of the scope of this work and thus, some examples have been sorted into groups of similar dimensionality.

1.3.1 3D Perovskite related phases

The group of 3D perovskites comprises amongst others: the inverse perovskites,[33, 34] the ReO_3[35] and WO_3[36] (that can be considered as A site deficient perovskites □BX_3), as well as the hybrid organic/inorganic phases (see Fig 5).

Anti-perovskites are compounds of general composition A_3BX where the anion becomes the centre of the octahedra and can form either the cubic or the hexagonal perovskite derivates. Regarding the hybrid perovskites, changing or combining different (organic) molecules has been used to reduce the dimensionalities down to 2 or 1 (see 1.3.1 and 1.3.2).[37, 38]

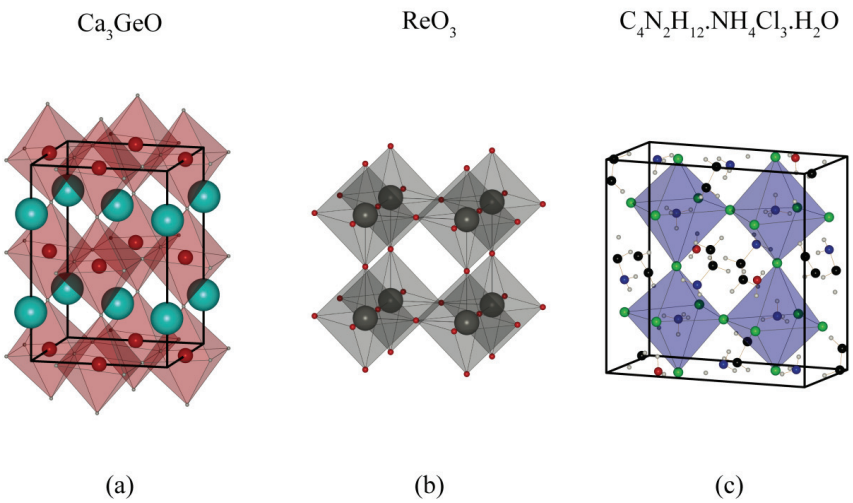

Fig 5. 3D Perovskite related phases. (a) Structure of the anti-perovskite Ca_3GeO adopting an anti-$GdFeO_3$ structure. (Ca in grey, Ge in Turquoise, O in red).[34] (b) Structure of ReO_3 (Re^{6+} in Grey, O^{2-} in red).[35] (c) Cubic hybrid structure $C_4N_2H_{12}.NH_4Cl_3.H_2O$ ($C_4N_2H_{12}^{2-}$ on A site, NH_4^+ on B site, Cl^- on X site. C in Black, H in white, N in blue, O in red and Cl in green).[38]

1.3.2 2D Perovskite related phases

Two dimensional phases are very frequent in the perovskite related phases, and occur upon ordering of anion vacancies as in Fig 4(d) or when off-stoichiometry induces ordered planar defects. This dimensionality can have interesting effects on the conduction of ions or

electrons and magnetic anisotropy caused by the alternation of planes with different types of atomic and electronic structures. Additionally, the interlayer is well suited for intercalation reactions of water, CO_2 and other ions.[39-44]

As mentioned above, the dimensionality can be induced when there is an off stoichiometry either on the anion site or on the cationic site of a perovskite layer. When this happens, intergrowth structures between perovskite blocks and a second structure type or between two perovskite (-related) structures can be observed. In the former case, three widely studied structure families are found :

- The Aurivillius phases[45-47] $(A'_2X_2)(A_{n-1}B_nX_{3n+1})$.
- The Dion-Jacobsen phases[48, 49] $A'(A_{n-1}B_nX_{3n+1})$.
- The Ruddlesden-Popper phases[50, 51] $(A'X)(ABX_3)_n$.

Fig 6 shows the structure for each of them.

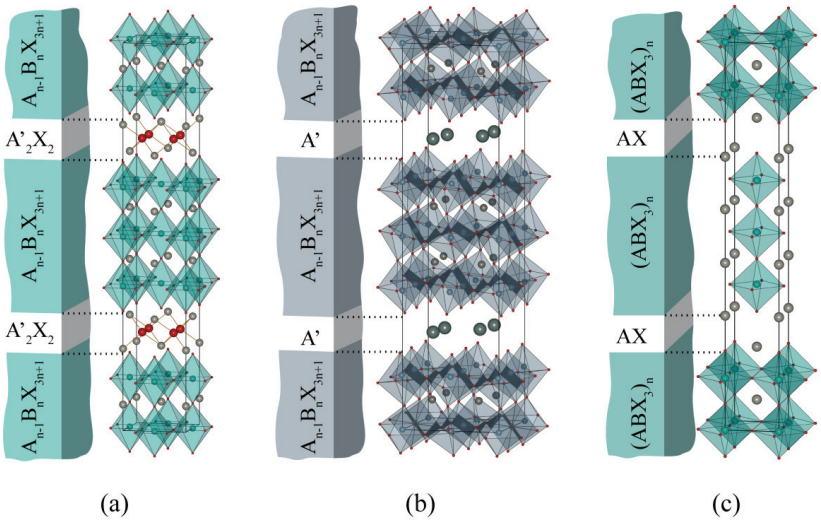

Fig 6. 2D Perovskite related structures: Aurivillius, Dion-Jacobsen and Ruddlesden-Popper intergrowth structures where n=3. a) The structure of the Aurivillius phase $Bi_2O_2Bi_2Ti_3O_{10}$ (Bi, Ti and O atoms respectively coloured in grey, turquoise and red).[46] b) The structure of a Dion-Jacobsen phase $CsCa_2Nb_3O_{10}$(Cs, Ca, Nb and O atoms respectively coloured in dark grey (large spheres), lighter grey (small spheres), pale blue and red).[52] c) The Ruddlesden-Popper phases $Sr_4Ti_3O_{10}$ (Sr, Ti and O atoms respectively coloured in grey, turquoise and red).[53]

In the Aurivillius phases, an excess of a heavy cations on the A site forms layers of A'_2X_2 that alternate with layers of perovskite blocks causing these to shift relative to each other by a vector $[½, 0, 0]_p$. The first reporting of the Aurivillius phases with n=3, 4 and 5 contained exclusively Bi^{3+} cations on both the A' and A sites. Since, phases with n values up to 8[54, 55] have been synthesised. Furthermore, in order to tune their properties, numerous substitutions have been performed within the perovskite blocks by elements from the alkali metals, alkaline earth, rare earths, and later metals from group XIV such as Pb and Sn on the A sites. Whereas on the B site, many 3d and 4d transition metals have successfully been co-substituted or even entirely replaced Ti[54, 56]. Additionally evidence of substitution of Bi^{3+} by Pb^{2+} within the $[Bi_2O_2]^{2+}$ sheets upon doping has also been shown[57, 58].

The Dion-Jacobson phases were first described by Dion[48] for n=3 and contained a monovalent alkali cation or NH_4^+ on the A' site. Jacobson[49] further extended this family of compounds by increasing the number "n" of stacked perovskite unite cells in the $A_{n-1}B_nX_{3n+1}$ slabs from three to seven. The A site is usually occupied by an alkaline earth metal but can also accommodate rare earth cations.[59] The B site is usually occupied by Ti, Nb or Ta.[60] The compound is very versatile and has been used for intercalation of organic compounds and ion exchange.[61-64] Lichtenberg distinguishes three types of Dion Jacobson structures according to the displacement between the perovskite slabs. The first, has a direct sacking of the blocks (i.e. the octahedra are stacked directly over each other). In the second, the slabs are displaced with respect to each other by a $[½00]_p$ vector and finally, in the third type of stacking, two successive perovskite slabs are shifted by a vector $[½½0]_p$ with respect to each other.[60]

Ruddlesden-Popper phases can be synthesised with relative ease for the first three members of the series (see Fig 7) as bulk compounds and encompass a wide variety of compositions[60]. On the A site, elements from group I, group II, rare earths, Y, Bi, etc..., can be present alone or as solid solutions. Whereas on the B site, most elements from the 3d and 4d transition metals, some group XIII and XIV elements and even carbonate groups[65, 66] can be incorporated. When RP phases contain group I elements, these are often ion exchanged with other mono and divalent metals. This has led to structures where the A site were ion exchanged with much smaller transition metals but yet, retained high stability[67]. When reduced, they can also accommodate $(OH)^-$, H_2O and CO_3^{2-}/CO_2 within the interlayer. However for these intercalated compounds, the exact location and ordering of the molecules within the AX layer is still subject to some debate.[40]

Recently, through thin film techniques, higher order members (n=4, 5 and 6) were successfully synthesised[68, 69] and has allowed the synthesis of RP phases where the perovskite slabs are A site ordered.[69]

Similar to the Dion-Jacobson phases where the A:B ratio is 1:1, a second class of 2D compounds exists with A:B ratio of 1:1. However in these compounds, while the unity A:B ratio is preserved within the perovskite slabs, the total cation to anion ratio is smaller and its generic chemical formula is written as $A_nB_nX_{3n+2}$.[70-73] They also differ in the structure of the slabs themselves. Whereas in the 3 aforementioned cases, the "n" ABX_3 perovskite units are contained in a slab stack parallel to a_p (i.e. long crystallographic axis **c** // to $[100]_p$), in the case of the "3n+2" compounds, the slabs are formed of "n" ABX_3 units that are stacked along their face diagonal (i.e. long crystallographic axis "**c**" // to $[110]_p$).

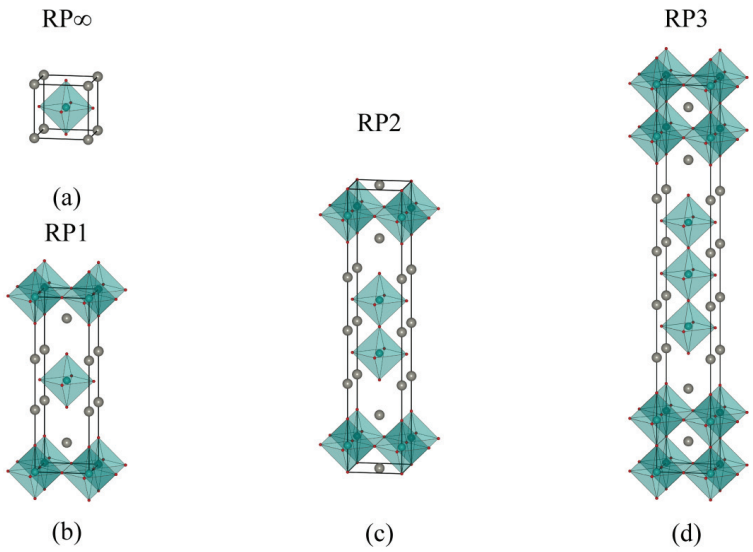

Fig7. 2D Perovskite related structures: RPn, the Ruddlesden-Popper series. (a) The RP∞, the ideal perovskite $SrTiO_3$. (b) Sr_2TiO_4, an ideal RP1 with alternating ABX_3 and RS layers. (c) $Sr_3Ti_2O_7$, an ideal RP2 where RS layers alternate with ABX_3 slabs 2 unit cells thick. (d) $Sr_4Ti_3O_{10}$, an ideal RP3 structure with alternating RS and triple ABX_3 layers.[50, 51]

Additionally, the ordering of the A and B defects in planes causes the ABX_3 slabs to shift with respect to each other by half a primitive unit cell in both "**a**" and "**b**" directions. (See Fig 8 (a)). From a compositional point of view, these phases have been reported for "Ti", "Nb" or "Ta" occupying 67% or more of the B sites. The remaining 33% support substitutions of these

three metals by various transition and other metals. On the A site, they are reported to accommodate alkali metals, alkaline earths, rare earths and Pb. Remarkably, these structures can present alternations of two members over long distances leading to average non integer values of "n"[60, 74].

A family of 2D perovskite related materials that has proved to be of fundamental importance is that of the layered cuprates. To date they are still the materials reported to have the highest critical temperature for superconductivity. Though some such as $La_2CuO_{4+\delta}$[75] adopt the RP1 structure, others such as the "YBCO-123"[76, 77] compound $YBa_2Cu_3O_7$ are directly perovskitie related. Nevertheless a common feature amongst all the superconducting cuprates is the presence of conducting blocks that are separated from each other by insulating layers. The entire structure can thus be represented by up to four different structural components: a conducting CuO_2 sheet, a separating layer and a spacing layer form the conducting blocks that are separated from each other by an insulating layer (respectively the turquoise, green, black and red arrows in Fig 9 (b)). These features were used as a basis for the four digit classification scheme of these compounds.[78] In this scheme, the first digit represents the number of insulating sheets containing heavy metal atoms (such as Bi, Hg, Pb, Tl, or Re) between two adjacent conducting blocks. The number of spacing layers that occur between identical CuO_2 containing blocks is given by the second digit and must be equal to twice the amount of conducting blocks. The third digit gives the number of layers that separate the CuO_2 sheets within a conducting block (i.e. the "separating" layers). Both the spacing and the separating layers typically contain lanthanide or alkaline-earth elements. In the case of the former, they form "AO" layers that take the rock salt structure when no insulating layer is present, thereby linking the RP1 superconducting cuprates to the other compounds.[7]

Using this classification scheme, the RP1 $La_2CuO_{4+\delta}$ is classified as a 0201T structure where the added suffix "T" is used to describe the oxygen environment in a given family and corresponds in this case to an octahedral environment. Similarly the well known $YBa_2Cu_3O_7$ compound traditionally referred to as the YBCO-123 is classified as a 1212C compound. In this case the suffix reflects the presence of insulating "Cu-O" chains.

Within all of these structures, additional variability due to the ordering schemes of cations (as exemplified in the high temperature superconducting cuprates) or anion vacancies, the tilting of coordination octahedra[79-81] should be kept in mind when investigating them. Thus, the family of 2D-layered perovskites is still in constant growth with novel ones still being synthesised. Examples of such phases are represented in Fig 9, where, in (a), an intergrowth

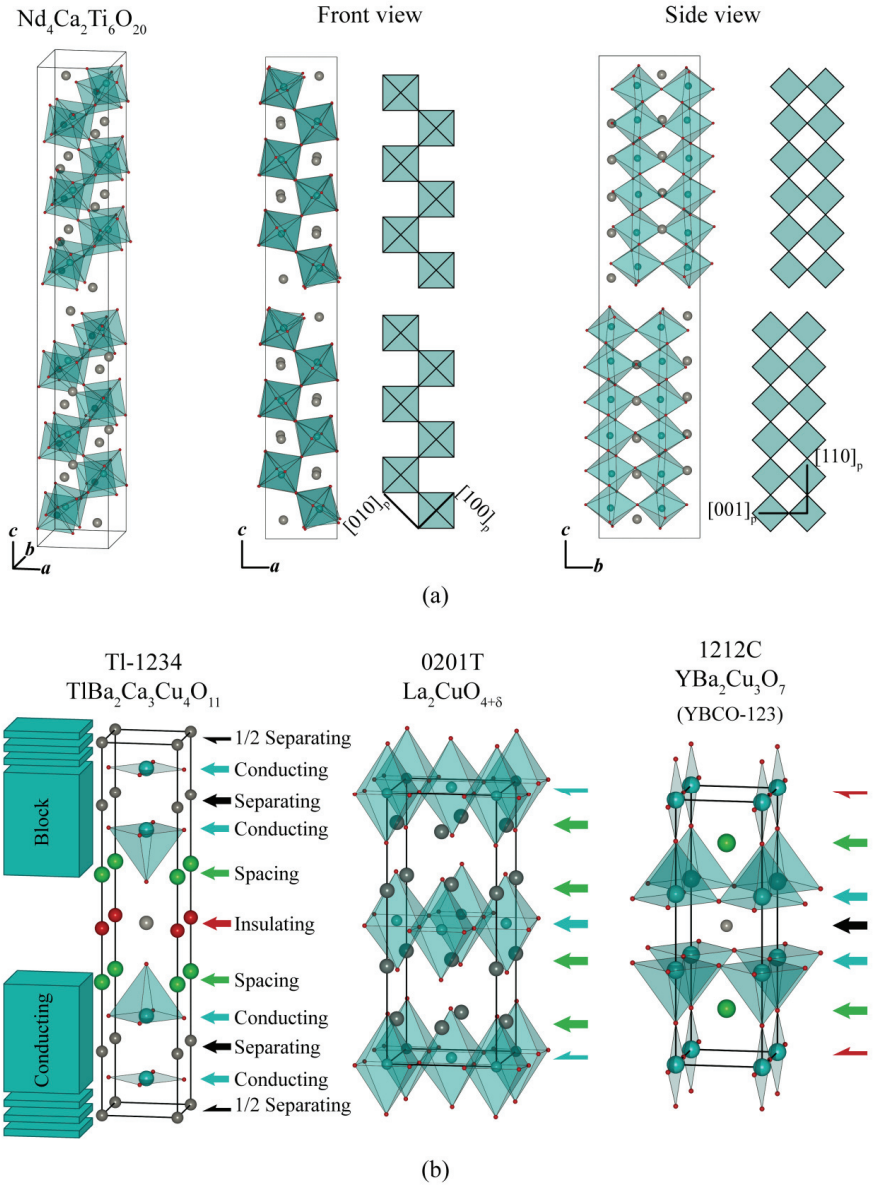

Fig8. 2D Perovskite related structures: "3n+2" perovskites, The high T_c superconductors. (a) From left to right: a projection of $Nd_4Ca_2Ti_6O_{20}$ an $A_nB_nO_{3n+2}$ phase where n=6,[82] the planar projection of the "front" ***ac*** plane of the structure, a schematic representation showing the stacking sequence along the perovskite face diagonals in the ac plane, a planar projection of the "side" ***bc*** plane and a schematic representation showing the linking of the individual perovskite units along a $[001]_p$ axis within the blocks (b) Superconducting cuprates: left a "12(n-1)n" compound with n=4, $Tl_1Ba_2Ca_3Cu_4O_{11}$ (Tl, Ba, Ca, Cu and O respectively in grey (big), green, grey (small), turquoise and red) centre the $La_2CuO_{4+\delta}$ a 0201T structure (La, Cu and O respectively in grey, turquoise and red) and right the structure of $YBa_2Cu_3O_7$ (Y, Ba, Cu and O respectively in grey , green, turquoise and red) part of the 1212T compounds.[83-85]

of two defect perovskite related phases with $Ca_2Fe_2O_5$ and $YBaFeO_5$ structures was first synthesised by Tenailleau et *al*.[86] then further investigated by Demont et *al*.[87] In Fig 9 (b) and (c), the possibilities for synthesising diverse structures offered by novel hybrid materials is shown. In such structures organic linkers may separate stacks of perovskite layers oriented according to the $[100]_p$, $[110]_p$ or $[111]_p$ directions[37, 88]. These can be represented respectively by the "$(RNH3)_2\ A_{n-1}\ M_nX_{3n+1}$" (with e.g. R=$C_4H_9$, A=$CH_3NH_3^+$, M=Sn and X=I), the "$A'_2A_nM_nX_{3m+2}$" (with e.g. A'=$NH_2C(I)NH_2^+$, A=$CH_3NH_3^+$, M=Sn and X=I) and the "$A'_2A_{n-1}M_nX_{3n-3}$" formulae. Whereas in Fig 9 (d), the presence of a 2D anti-perovskite phase adopting an anti-K_2NiF_4 structure shows that 2D ordering is possible in such compounds as well.[89, 90]

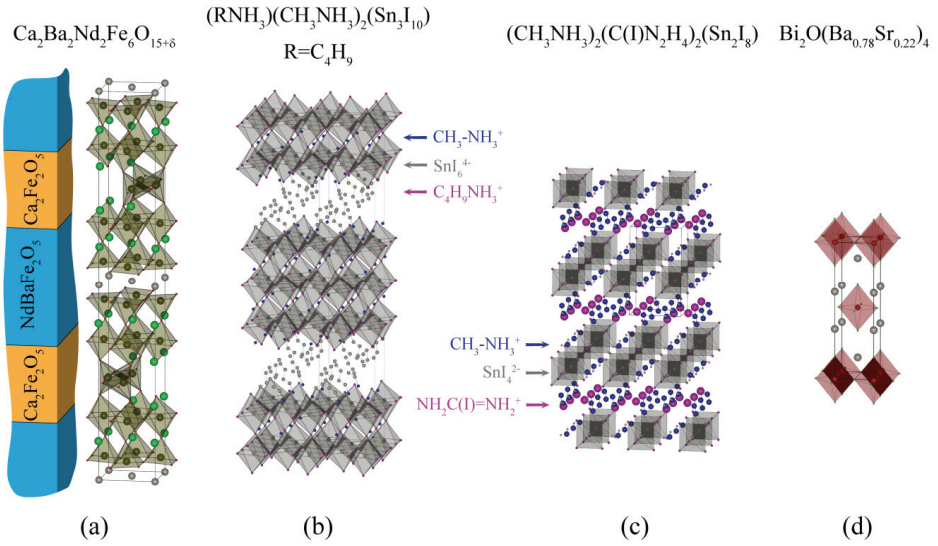

Fig9. 2D Perovskite related structures: Perovskite related intergrowths, hybrid systems and layered anti-perovskites (a) Intergrowth between a "$Ca_2Fe_2O_5$" -type phase and a "$NdBa_2Fe_2O_5$" -type phase.[86] (b) and (c) Hybrid organic-inorganic layered structures with $[100]_p$ (i.e. $((CH_3)NH_3)_2((C_4H_9)NH_3)_2(Sn_3I_{10})$) and $[110]_p$ (i.e. $((CH_3)NH_3)_2(C(I)N_2H_4)_2(Sn_2I_8)$) stacking of the ABO_3 units.[91, 92] (d) The layered anti-perovskite $(Ba_{0.78}Sr_{0.22})_4Bi_2O$ with inverse K_2NiF_4 structure (O atoms in red, Bi atoms in Grey and Sr and Ba atoms in green).[89]

1.3.3 1D Perovskite related phases

Perovskite related materials with a 1D structure are formed when the coordinating octahedra of the "B" cation form chains. This happens in hexagonal perovskites that typically contain a

large A cation and small B cation. Such cases are characterised by a tolerance factor greater than 1. The AX_3 closed packed layers can then organise themselves according to an "hcp" stacking where the BX_6 octahedra are found in a face sharing configuration. As a consequence, the B-B distances become shorter and cationic repulsion start to occur. In compounds such as $BaFeO_3$ (fig 1c) the hcp stacked AX_3 layers alternate with ccp layers in order to diminish this repulsion. In others, the B-B inter-atomic repulsion can be alleviated by the formation of a B-B bond (eg. $BaRuO_3$). When only hcp packing of AX_3 layers subsist then one gets the 2H polytype (eg. $BaNiO_3$) where the face sharing $[NiO_3]^{2-}$ octahedra form chains (see Fig 10 (a)). Such chains of face sharing polyhedra are also found in the $A_{1+x}(A'_xB_{1-x})O_3$ compounds (eg. $Sr_4Ru_2O_9$). These form a wider series of materials of general formula $A_{3n+3m}A'_nB_{3m+n}X_{9m+6n}$.[93] The two end members correspond to the 2H ABX_3 (n=0 m=1) structure and the Sr_4PtO_6 structure (n=1, m=0) (Fig 10 (b)).

Another way of achieving chains is to dilute the octahedra within an organic environment (Fig 10(c)). This was shown to happen notably for the first members (i.e. n=1)[37, 88] of the systems that form the aforementioned 2D structures with stacking of ABX_3 units along the [110]p and [111]p directions.

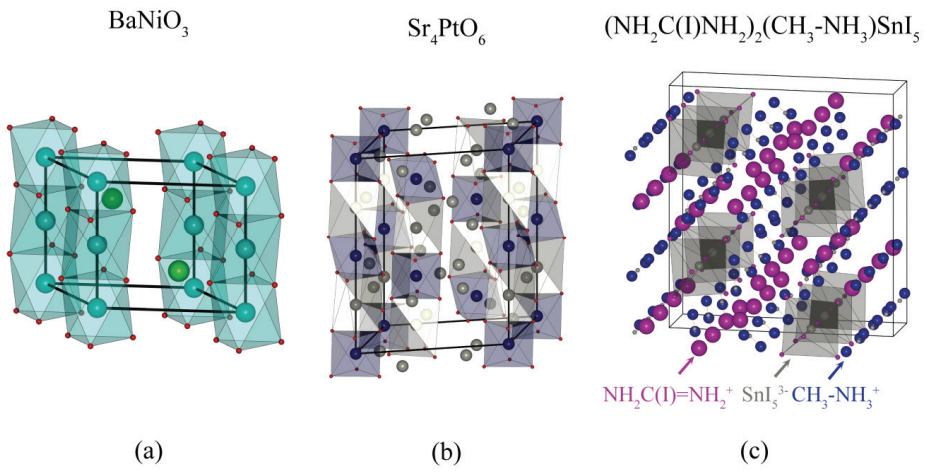

Fig 10. 1D Perovskite related structures. (a) The 2H hexagonal perovskite $BaNiO_3$, an example of a columnar perovskite structure (Ni atoms in light blue, Ba atoms in green and O atoms in red).[94] (b) The Sr_4PtO_6 structure with Sr cations in prismatic environment linking 2 PtO_6 octahedra.[95] (c) 1D hybrid structure from the A [110]p stacked series. [96]

As a final note to this section, more complex phases can readily be obtained by direct synthesis or post treatment leading to combination of e.g. RP3 phases with brownmillerite structures[97]. It should therefore not be unexpected to see in the future specific A, B and X ordering schemes permitted by non conventional synthesis methods and by the spreading of thin film techniques and other "bottom-up" synthesis methods. This holds the promise for a greater understanding of fundamental properties of materials as well as their tailoring through a near infinite combination of the structures presented above.

1.4 Perovskites and their applications.

As illustrated earlier by the case of the $AFeO_3$ compounds (see 1.1), the properties of perovskites can vary widely not only due to compositions but also due to their structure. This leads to many possible applications in many domains. Throughout the following section of the chapter, a selection of these will be described with a particular focus on the application of perovskite oxides. The application areas have been divided into two subgroups based on the temperatures at which technological interesting phenomena occur.

1.4.1 From high- to room- temperature.

1.4.1.1 Catalysts.

Perovskites with B^{3+} transition metals have been widely studied as catalysts from room to elevated temperatures for which several books and review articles can be found.[98-101] They have in particular been suggested for the elimination of un-burnt pollutants from exhaust gases (CO, NO_x,...), for oxidative coupling reactions and for partial oxidation of hydrocarbons in systems that have separate reaction and catalyst regeneration steps.[98, 99, 102-106] The adsorption of these pollutants gases have been shown to occur via surface defects on the perovskite and more specifically through the oxygen vacancies [107] (Fig 11 (a)) though once adsorbed, they may diffuse towards the bulk of the material through structural vacancies[108, 109]. The structural and compositional versatility of the perovskite and related structures allow for the tuning of the acidity/basicity as well as the redox properties of the catalysts. The former is widely affected by the composition and can be evaluated using the concept of "optical basicity as has been defined by Duffy et al.[110-112] The latter is essentially dependant of the B site composition and its interaction with the anion as this determines the electronic structure at and around the Fermi level. This fine tuning allows the targeting of the specific surface and bulk conditions to ensure selectivity with respect to the desired products.[113, 114] They are particularly well suited with the use of (semi-)noble metals such as Rh and Pd that can be

incorporated in the structure upon an oxidation step then regenerated as nanoparticles in a reduction step. This has the advantage over the classical metal supported catalysts (e.g. Pt-Rh/Al_2O_3,...) of preventing the metal nanoparticles from sintering (see Fig 11(b)). Such "intelligent catalysts" consequently lead to more and smaller nanoparticles when in use. Put in other terms, this leads to a higher number of active surface sites and extended catalyst life upon cycling.[99]

As examples, one may site systems such as $La_{0.6}Sr_{0.4}Co_{0.8}Fe_{0.2}O_3$ (LSCF) that have been studied for the oxidative coupling of CH_4 to C_2H_6 and C_2H_4.[115] This system provided decent selectivities towards C_2 molecules (up to 67%). For this, the reactor was configured as a catalytic membrane reactor, where the CH_4 is separated by the perovskite membrane from the stream of oxygen/air. A possible configuration of such a reactor is shown in Fig 12 (a)).

Other perovskite systems have been studied for the partial oxidation of CH_4. Recently, by testing the Rh-LSCF and Rh-LSCFA (i.e. Rh/Rh_2O_3 on $La_{1-m}Sr_mCo_{1-x-y}Fe_xAl_yO_{3-\delta}$)[116] perovskites catalysts supported by Al_2O_3 it was shown that, after initial activation of the catalyst, the CH_4 molecules activated by the Rh nanoparticles consumed bulk oxygen from the perovskite for the partial reduction to syngas. Such systems offer innovative solutions notably for the offshore conversion of methane.

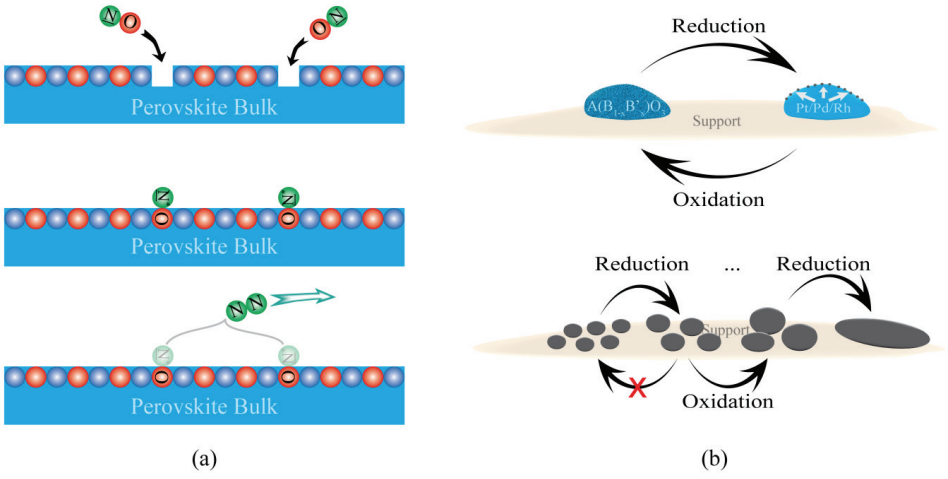

Fig 11. Perovskite as (co-) catalysts. (a) Surface reaction scheme of NO with the surface of a perovskite catalyst. (b) Schematic representation of the nanoparticles creation of metal nanoparticles from an ABB'O3 perovskite (eg. B'= Pt, Rh or Pd) supported particle upon cycling between oxidising and reducing conditions (upper cartoon) and irreversible sintering of the noble metal nanoparticles with successive cycling (lower cartoon).

Furthermore perovskite related materials have been suggested as photocatalysts for water splitting reactions. Most notably the Aurivillius and Dion-Jacobsen phases have been extensively studied for such applications.[117, 118]

As a final example, it has been suggested that perovskite catalysts could also be integrated to sensors for in-situ process monitoring.[119]

1.4.1.2 Membranes

The Oxford English Dictionary defines the word "membrane" as: "Any thin, often pliable, sheet or layer, especially one forming a barrier or lining." As such perovskites and their related materials have been widely studied as barriers that may selectively conduct a targeted ionic species. Most of the studies to date have focused on oxide-ion and proton conducting membranes as evidenced by the wide amount of reviews on the subject.[54, 120-124] Since the early 1990's however, attention has been focussing on the perovskite $Li_{3x}La_{(2/3)-x}\square_{(1/3)-2x}TiO_3$ (LLT) which to date has one of the highest Li-ion conductivities for solid electrolytes.[125-127]

From an application perspective, mixed ionic and electronic conductors (MIEC) are distinguished from the purely ionic conductors. MIEC's have been studied for uses in catalytic membrane reactors (e.g. LSCF [115]), gas separation membranes[128] or as electrodes for fuel cells[129-131] whereas ionic conductors have been proposed as solid electrolytes for batteries and fuel cells[132, 133]. Synthesis of new materials need to meet the required conditions of long term stability (both mechanical and chemical) and catalytic activity and conductivities over a wide range of temperatures specific for each of these applications.

As an example, Fig 12 (b) shows the two types of fuel cells where perovskite and related materials can be found. In the upper part representing the functioning of a solid oxide fuel cell, a MIEC is used as cathode to convert the oxygen from the air into lattice oxygen. Typically the LSCF, BSCF ($Ba_{1-x}Sr_xCo_{1-y}Fe_yO_3$), RP phases, some Co doped lanthanum nickelate perovskites and others have been studied. From the cathode, the oxide ions travel through the electrolyte towards the anode material. Traditionally, oxides such as Y stabilised ZrO_2 or Gd doped CeO_2 have been used as electrolytes. However perovskites from the La-Sr-Ga-Mg-O system have also been studied as for this purpose. Finally at the anode, the O^{2-} reacts with the hydrogen to form water.[134, 135]

In the lower part of the scheme, a proton exchange membrane fuel cell is depicted. In this case, rather than having the oxide ion move through the cell, protons are generated at the anode and migrate through a proton conducting electrolyte towards the cathode where it reacts with

oxygen to form water. Perovskite materials studied for such fuel cells comprise mainly of the proton conductors ($SrZr_{1-x}Y_xO_{3-\delta}$ and $BaCe_{1-x}Y_xO_{3-\delta}$) used as electrolytes.[136, 137] Some of the studied cells used the aforementioned perovskites as cathodes and cermets (i.e. Ni/ABX_3) as anodes.[134]

For both functioning modes, the electrons flow through an external circuit from the anode to the cathode. This current can then be used as automotive or stationary power sources.

1.4.1.3 Thermo-electrics

When two dissimilar materials are joined together and subjected to temperature difference between the junction and the ends, then a potential difference can be observed between two sides that is proportional to the temperature difference. This effect, was first observed by TJ Seebeck[138] and has been named after him. It can readily be observed in metals (couple of μV/K) and semi conductors (couple of 100μV/K).[139] Thermo electric materials are characterised by their Seebeck coefficient "α_{TP}" and by a figure of merit "ZT" (see eq(3)).

$$ZT = \frac{\alpha_{TP}^2 T}{\rho\kappa} \qquad (3)$$

Where "T" is the temperature in Kelvins, "α_{TP}" the Seebeck coefficient, "κ" the thermal conductivity (electronic and lattice contributions) and ρ the materials resistivity.

Therefore, in their continuous quest for new sources of energy, researchers have started to look at semi conducting oxide materials as candidates for thermo power generation. It derives from (3) that the ideal thermo electric material should have low resistivity, low thermal conductivity and a high Seebeck coefficient. As such perovskites [140-142] and their related phases (RP phases[140, 143], ...) have started to draw interest as novel thermoelectric materials due to the possibilities that they offer with respect to "engineering" of their band gap and thermal conductivities. State of the art figures of merit are in the range of 0.1-0.5 for these materials.[139] Fig 12 (c) shows the 2 possible modes for using thermoelectric materials: on the upper part, the thermoelectric couple is used for power generation between two temperature sources. The lower part shows the thermoelectric system used for active cooling of a hot component (i.e. refrigeration mode).

1.4.1.4 Other applications

Upon substitution of the oxide anion by a nitride anion, the band gap of the semiconducting perovskites is increased and the materials are characterised by bright and deep colours (e.g. yellow for $CaTaO_2N$ and red for $LaTaON_2$). Therefore, some have suggested the use of

perovskite oxi-nitrides as new pigments where toxic heavy metal cations could be replaced by cheaper and less toxic transition metals.[144]

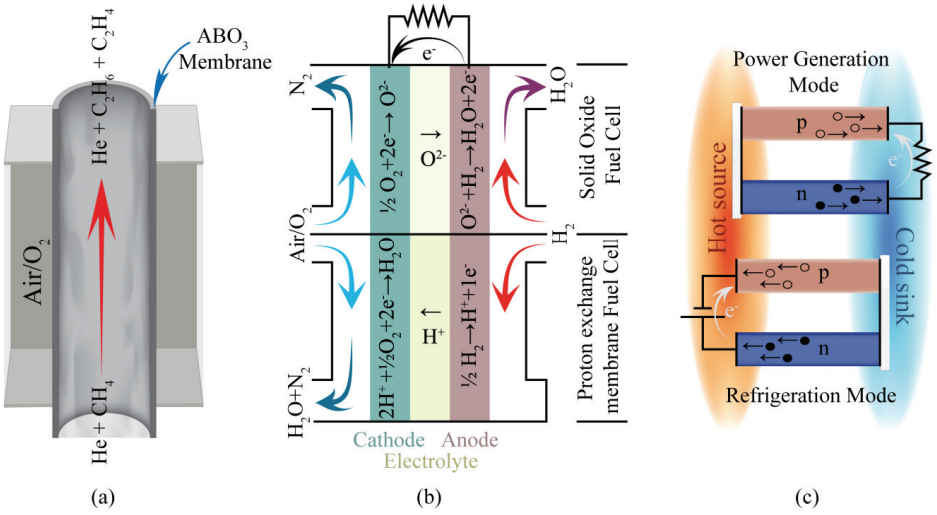

Fig 12. Application of perovskites from high to room temperatures. (a) As a catalystic membrane reactor. (b) As a fuel cell. (c) In a thermoelectric system.

1.4.2 From room- to low- temperature.

At elevated temperatures, energetic processes such as ionic conduction and, to some extent metallic conduction of electrons in large band gap semi conductors are activated by the thermal energy. As the temperatures are lowered, these processes start having a minority contribution to the properties. Therefore at lower temperatures, the properties of the materials start to be dominated by their electronic structures. In perovskite compounds, various theories have been developed a.o. by Mott[145], Goodenough and Kanamori,[146-149] Efros and Shkloskii[150] as well as Zaanen, Sawatzky and Allen[151] in order to rationalise the relations between the properties and the structures in Oxides. These theories permit the explanation of phenomena such as metal to insulator (MI) transitions, coupling of spins in AFM or FM alignments, variable range hopping (VRH), electronic structure of cations in high oxidation states etc... The applications of in the following section have been divided into subsections that focus on the electronic structure, magnetic structure and the combination of both of these aspects.

1.4.2.1 Perovskites for their electronic properties.

Around World War II, the rapid development of electronics for uses in communication technologies and consumer electronics led to the development of a wide array of materials. Notably, $BaTiO_3$ was widely used as a dielectric in capacitors and since, it has found applications in numerous other domains.[152] Structurally, the Ti^{4+} cations in $BaTiO_3$ are not centred within the $[TiO_6]^{2-}$ octahedron. This causes an electric dipole within the compound thereby lowering the structure's symmetry. More specifically, due to long range ordering of the dipole, the compound is more correctly classified as a ferroelectric (FE) material. As with their magnetic counterparts, these order parallel to each other within domains below a transition temperature and present a hysteresis when subjected to a varying electric field. In the case of $BaTiO_3$ this temperature is c.a. 390K. Other FE perovskites or related structures (mainly RP and Aurivillius type compounds) have been successfully applied as piezoelectric materials in transducers and actuators ($PbZrO_3$-$PbTiO_3$ solid solutions), high-κ dielectrics ($BaTiO_3$-$SrTiO_3$, $CaCu_3Ti_4O_{12}$) and as candidates for Fe-RAM technology.[153-158] Once more, all these properties can be tuned by the structural and chemical flexibility of perovskites to fit the requirements for specific applications. One may site the tuning of the FE transition temperature by co doping leading to "low loss" paraelectric materials (PE). More recent developments also include the search of lead free piezoelectric materials for sensors and actuators in micro electronics.[159]

Though many perovskites of technological interest are insulating, there are equally as many if not more that are either semiconducting or metallic. Much research has gone into understanding these compounds as they offer an insight into the underlying physics and the link between a material's structure and its properties. Additionally, through structural modifications, it is possible to observe gradual effects such as MI transitions that occur upon charge ordering (CO) or transitions from 3D to 2D VRH upon going from a perovskite to a layered structure.[14, 160, 161] As these effects occur simultaneously with many interesting magnetic phenomena, they shall be treated in more detail later (c.f. section 1.4.2.3)

1.4.2.2 Perovskites for their magnetic properties.

When inserted in a magnetic field H, the circulation of electrons within a material will create a field opposed to H. This is known as diamagnetism and is present in all materials. However, when there are unpaired electrons present in the valence band other phenomena may occur. At sufficiently high temperatures, the thermal energy supplants that of the inter electron spin interactions. The material is in its paramagnetic (PM) state. Upon sufficient cooling, the

electrons start to interact with each other aligning their spins parallel or anti parallel. These are respectively the ferromagnetic and anti-ferromagnetic interactions. When in a material they occur over large domains they are classified as ferromagnetic (FM), or anti-ferromagnetic materials (AFM). In addition to these basic long range magnetic configurations, two others are readily encountered in perovskites. Ferrimagnetism (FiM), or when two FM sublattices of different net moments interact antiferromagnetically with each other, and frustrated magnetism (also called spin glass - S.G.) when the electronic spins are only locally ordered (FM or AFM).[162] When perovskites incorporate magnetic transition metals, they may exhibit any of these four interaction schemes. The additional influence of internal or external stimuli such as substitutions, cation or anion deficiencies, temperature or pressure allow to switch between any of the five aforementioned magnetic states (i.e. PM, FM, AFM, FiM or SG). Such crossovers between magnetic states can be found in the $Sr(Fe_{1-x}Co_x)O_{3-\delta}$ or the $RE_{0.5}AE_{0.5}MnO_{3-\delta}$ (with RE and AE denoting rare- and alkaline- earth atoms) solid solutions. For these compounds, the progressive substitutions on the A or B site lead to a crossover from AFM to FM type interactions.[163, 164]

The magnetic interactions in perovskites were rationalised by Goodenough and formalized by Kanamori in the late 1950's and have since become known as the Goodenough-Kanamori rules.[146-149] These rules may be used for predicting the dominating interactions within perovskites under certain conditions. Firstly the electrons are assumed to be localised. Secondly, a virtual electron transfer should be possible directly between transition metal atoms (superexchange) or via a certain amount of covalence between the cation and anion bonds. If these conditions are met, then the rules can be summarised as: AFM interactions will occur between two half-filled orbitals whereas FM interactions will occur between an empty and a half filled orbital. $REFeO_3$ compounds provide a typical example of AFM ordering.[165] More complex AFM ordering schemes are found for example in the Manganites ($La_{1-x}A_xMnO_3$) where Jahn-Teller distortions of the Mn^{3+} cations balanced by certain amounts of Mn^{4+} cations lead to simultaneous Spin, Charge and Orbital ordering schemes.[147]

If the localisation criterion is not met, then the electrons in the conduction band will tend to align with each other leading to FM interactions. This effect was used to explain the crossover between the AFM to FM interactions as well as the change in conductivities observed upon Co doping in certain Fe^{3+}-Fe^{4+} perovskite systems (e.g. in $CaFe_{1-x}Co_xO_3$).[14, 166] For FiM interactions to take place, two magnetic lattices are required and this interaction can be found

in several double perovskite systems (e.g. La_2CrFeO_6), or systems where oxygen vacancies create two dissimilar sub-lattices (e.g.$Sr_3YCo_4O_{10+\delta}$).[167, 168]

S.G. phases have been reported for compounds where FM and AFM interactions compete. This may happen with e.g. doped manganates and cobaltates.[169-171]

Fig 13 shows cartoons illustrating the 5 magnetic interactions that may occur in perovskites simplified to a 1D case (a) and another representing the Goodenough-Kanamori rules for a 180° superexchange interaction (b).

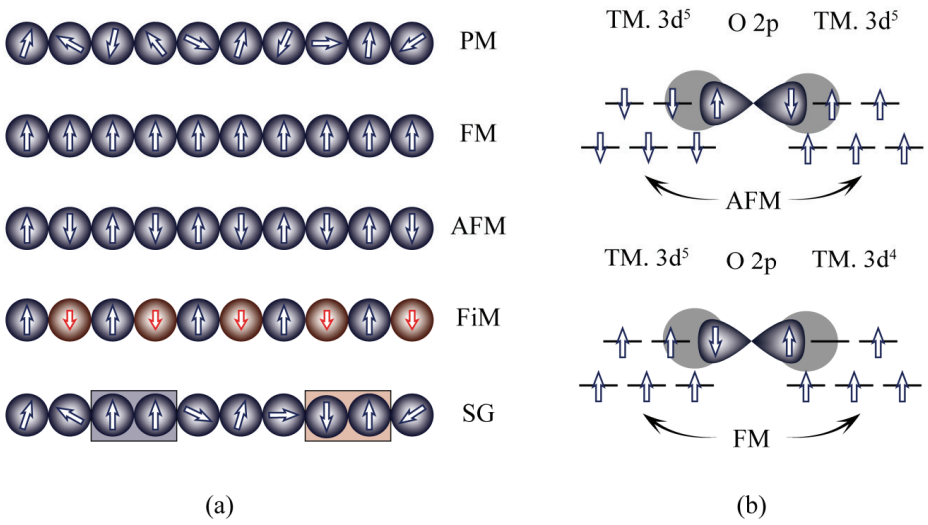

Fig 13. Magnetic interactions in perovskites. (a) The various possible magnetic interactions in a 1D chain of moments. Note the AFM interaction between two FM sublattices (blue and red)). For the SG interactions in a 1D chain, the areas of short range order are highlighted by boxes. (b) Superexchange interactions between spins on two $3d^5$ cations (upper) and between a $3d^5$ and a $3d^4$ cation (lower) mediated by the electrons on the 2p orbital of an oxygen due to bond covalency/overlap (grey circle).

1.4.2.3 Perovskites: combining magnetic and electric properties.

As exemplified in the two previous sections, both the electronic and magnetic properties of perovskites are closely correlated to their basic electronic structure. Therefore, any external stimuli that affect the basic electronic structure of the material will also influence either, or both, the electronic and magnetic properties. This has led to the discoveries of effects such as magneto resistance (MR), multiferroicity, half metalicity or superconductivity in perovskites,

their superstructures and perovskite related heterostructures.[172-175] In turn, these effects have led to candidate materials for applications within spintronics[176, 177] (for the reading and storing of data in magnetic form) and as high temperature superconductors.

MR was first observed by William Kelvin who experimented with currents flowing through ferromagnetic metals when placed in a magnetic field. He noted that resistance was at its peak when current and field were parallel to each other and at its minimum when they perpendicular. Around a century later three other MR effects were to be observed. The works by Grünberg and Fert[178, 179] led to discovery of an increased MR in multi layer films composed of ferromagnetic metal films separated by a non magnetic metal (Fig 14 (a)). This became known as "Giant Magneto Resistance" (GMR). Similarly, M Jullière discovered another MR effect, "Tunneling Magneto Resistance" (TMR), in heterostructures composed of ferromagnetic metals separated by semiconductors or insulators (Fig 14 (b)).[180] Both of these phenomena are based on the partial spin polarisation of the conducting electrons in ferromagnetic structures. This leads to an increased carrier transport (GMR) or increased tunnelling (TMR) when the FM domains are aligned parallel to each other.

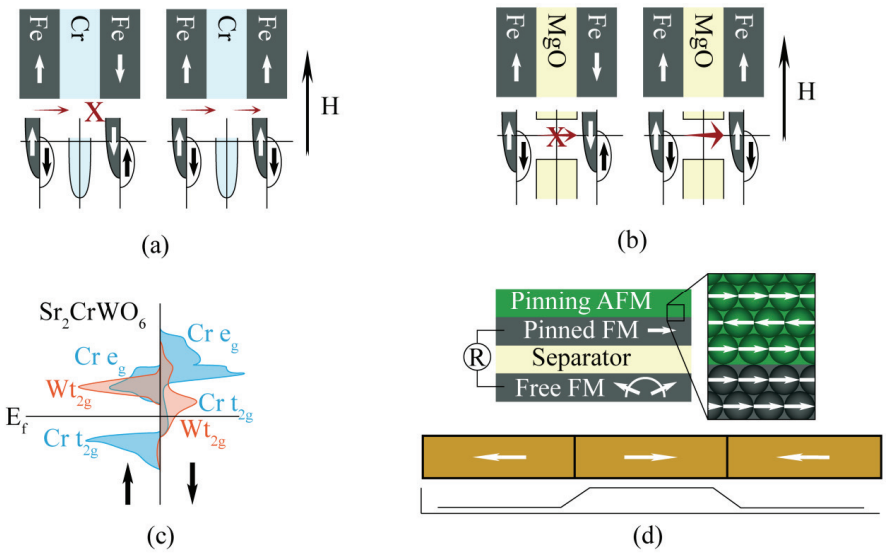

Fig 14 The MR effect and its applications. (a) A GMR heterostructure with AFM coupling of the FM layers. (b) A TMR. heterostructures with AFM coupling of the FM layers. (c) CMR: spin polarised band structure in the double perovskite Sr_2CrWO_6 after reference [181]. (d) Working principle behind GMR or TMR read heads: the spin valve.

The works of Jonker and van Santen on perovskite manganites[182, 183] led to the discovery of "Colossal Magneto Resistance" (CMR). It has been shown that for these and certain double perovskites a half metal structure may be created.[181, 184] In such compounds, the charge carriers are totally polarised due to a gap around the Fermi level for one of the spin orientations (Fig 14 (c)). Though magnetic interactions for the ground states of these manganites can be rationalised by M-O-M exchange interactions, these do not suffice for explaining the CMR effect. For this one needs to take into account the strong spin-phonon interactions that will affect the electronic structure of these materials.[172]

Both GMR and TMR structures, have found applications as "spin valves" notably in MRAM's and read heads in commercial hard disk drives. For example, in a G- or T-MR read head, one of the FM layers is pinned by depositing it on an AFM layer. The other FM layer, separated by a non magnetic metal or an insulator respectively, is free to align itself with the magnetic field generated by the domains on the media thereby affecting the resistance of the sandwich structure (Fig 14 (d)). Though CMR perovskites have not yet been used in these applications, the CMR effect is very sensitive for even small magnetic fields and offers promising prospects for spintronics.[176, 177, 184, 185]

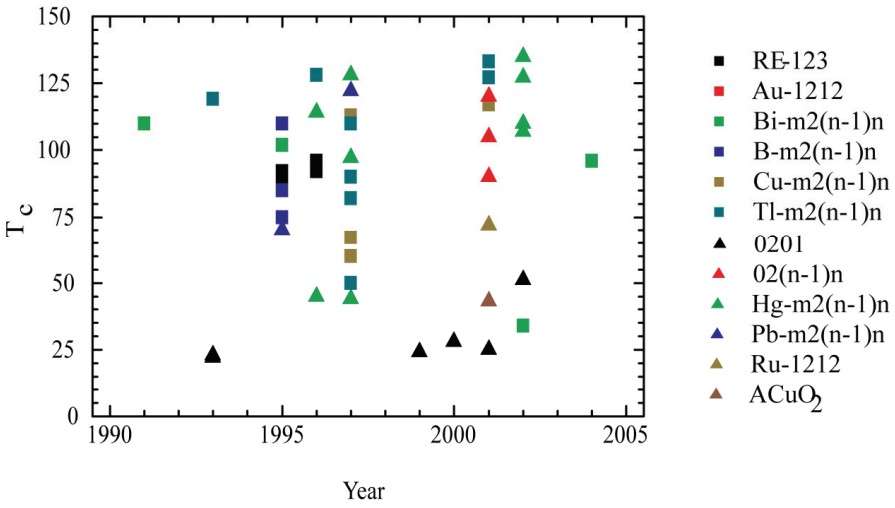

Fig 15. Status of the High Tc cuprate superconductors. Adapted from data in ref [186]

In point 1.3.2, mention was made of the High Tc superconducting oxides (H.T.S.C.). In Fig 15, one can see that critical temperatures of up to 135K have been obtained in these cuprates (the Hg-1223 compound) and that those with the highest Tc's are part of the "*m2(n-1)n*" family. All of these phases can be considered as charge carrier doped Mott insulators (i.e. compounds where the Coulomb interactions between charged particles open a gap at the Fermi-level). A significant development to H.T.S.C:'s was further made in 1994 by Maeno *et al.* who were the first to report superconductivity in a non Cu containing oxide: un-doped Sr_2RuO_4.[187] Despite having a very low Tc of c.a. 1K, this led to further developments in search of alternative H.T.S.C. phases. Since then superconductivity has been found in various other classes of layered compounds such as Fe- chalcogenides and pnictides.[188, 189] These have been the main focus of the research in H.T.S.C. for the last years.

1.5 Scope of this work.

This project "Novel oxides with interesting ionic, electronic and/or magnetic properties" was set up as a collaborative effort between the universities of Caen (Crismat), Liverpool (UoL) and Oslo (UiO) under the EU FP6 framework as a Marie Curie Early stage training network (MC-EST). Therefore the scope of this doctoral training was twofold:

Firstly, as suggested by its title, it aimed at studying new inorganic oxide materials for applications within energy (i.e. ionic and electronic properties) and data (i.e. electronic and magnetic) using both classical and new methods of synthesis and characterisation.

Secondly, as a MC-EST, it aimed at promoting the mobility of young researchers so that they may extend their knowledge, skill base and provide them with an international network.

For this thesis, the choice to work with perovskite related structures over the vast extent of available oxide structures arouse from their flexibility as well as from their current and potential technological importance. Indeed, they are already present in critical applications for modern day life that range from areas within energy technologies through transport and catalysis all the way to microelectronics. More importantly, they still offer exciting prospects both for our fundamental understanding of certain physical phenomena as well as for new applications as exemplified throughout the introduction. Furthermore, focusing this work on "layered" or complex intergrowth structures has the benefit of adding an additional spatial parameter to the compositional variables available for study. This additional parameter has been shown to have drastic effects on the electronic and ionic properties of the materials. To stay in line with the project description, it was decided to base this work on substituted

layered ferrates. The Fe- based perovskites are renowned for their stability in reducing atmospheres, their structural flexibility and interesting magnetic properties (Fe is a magnetic cation in all of its common oxidation states). Tailoring these structures and their properties by substitution of the Fe with other transition metals, co substitution of the "A" site and intercalation of guest molecules all create novel oxides with interesting ionic, electronic and magnetic properties.

Nevertheless, even with these criteria fulfilled, the variables to study remain plentiful. Therefore, the Ruddlesden Popper intergrowths with triple perovskite layers were chosen for their novelty and the potential for making a significant contribution on these oxides. The remaining of this dissertation focuses on the study of substituted RP3 ferrates through a detailed investigation of their structural behaviour and properties upon doping and insertion of chemical species at high-, room- and low- temperatures.

2 Materials and methods.

The following chapter constitutes a brief review of the methods used during this work for synthesising and characterising RP3 materials. These methods will be described and their use in this work explained.

2.1 Synthesis Methods.

All the synthesis methods used were aimed at producing crystalline solids in form of powders or pellets (depending on the methods used for further characterisation).

Classically three methods of choice exist for the synthesis of polycrystaline samples of perovskites and related compounds in bulk:

- The “solid precursor route” (a.k.a. “Shake and Bake”).
- The “co-precipitation” route.
- The “Sol-Gel” route.

The first is based on the thermal diffusion of cations and anions at elevated temperatures. It requires fine grinding (by hand or mechanically) of solid binary oxides or carbonates of the cations of interest, peletising the mixed powders and subsequent annealing(s). In order to achieve “X-ray” homogenous samples, high temperatures and multiple grindings are required. Nevertheless, in the case of (metal-) oxide mixtures, the method presents the advantage of being able to directly perform reactions in sealed or inert environments without needing to burn-off any volatile ligands.

The last two techniques are solution based and result in fine powders that present a better initial mixing than that which may be achieved by manual grinding. This presents, at the cost of an extra calcination step of precursor powders, the advantage of shorter diffusion lengths for the cations. Thus these methods require lower temperatures and present better sintering characteristics.

Over the course of this work, samples were prepared using the first as well as two different sol gel methods: the EDTA method and the citric acid method. Kakihana has written a comprehensive review of the various “Sol-Gel” methods that might be considered for the synthesis of perovskite related phases.[190]

Both the EDTA and the Citric acid methods are based on the formation of cation complexes in the solution (Sol-) before the onset of jellification (Gel). They differ mainly by the

chelating agent used (i.e. respectively ethylene diamine tetra-acetic acid and citric acid). When using either method, the cations are mixed on an atomic level prior to jellification. The obtained gels are then calcined between 400°C and 500°C in an oxidative environment. This last step is required to burn off the excess chelating and jellification adjuvants, after which amorphous powders are usually obtained.

The specifics of the final annealing steps and synthesis methods used can be found in the experimental section of the publications or will be specified when required for unpublished results.

In the second paper, hydration experiments on reduced RP3 phases were performed in a semi-closed system (see Fig. 16).The sample was place over a water bath and then covered to ensure a constant vapour pressure in the sample area. A small venting pipe permitted expansion of the gasses thereby maintaining a constant pressure while heating the water bath.

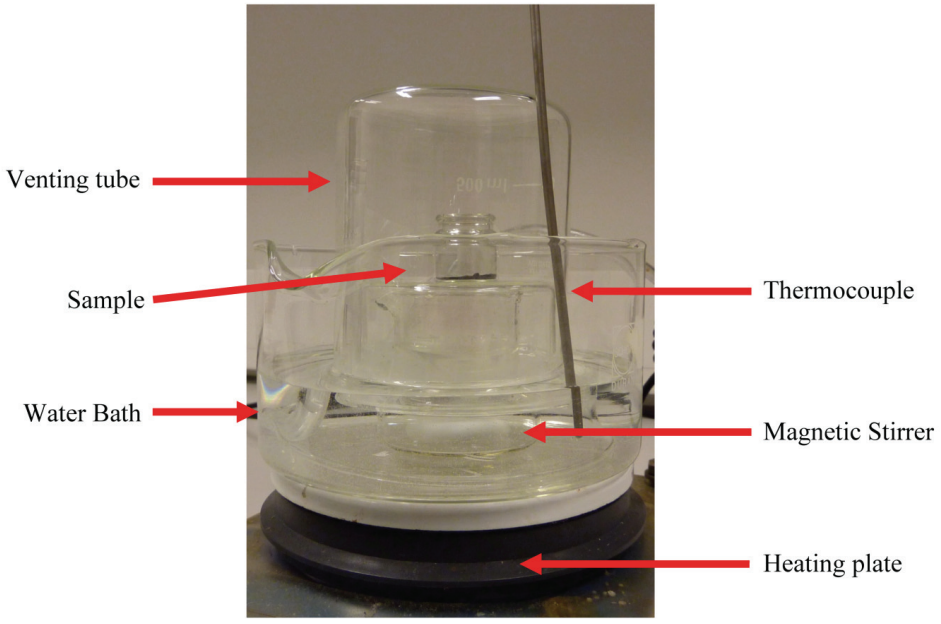

Fig 16. Hydration setup. Picture of the experimental setup used for hydration of samples at room and moderate temperatures.

2.2 Characterisation methods.

2.2.1 Chemical methods.

Cerimetric titration was used to determine the oxygen content of fully oxidised RP3. samples at room temperature (RT). This method is highly suitable for the redox titration of high valent Fe and Co cations. It is based on the reactivity of Fe^{2+} cations coming from an external salt (Fe^{2+}_{Salt}), with high valent Fe^{4+}, Co^{3+} and Co^{4+} cations from the sample to form Co^{2+} and Fe^{3+}. (equations (4) to (9)).

$$Fe^{2+}_{Salt} + Fe^{2+}_{Sample} \rightarrow 2Fe^{2+}_{Solution} \quad (4)$$

$$Fe^{2+}_{Salt} + Fe^{3+}_{Sample} \rightarrow Fe^{2+}_{Solution} + Fe^{3+}_{Solution} \quad (5)$$

$$Fe^{2+}_{Salt} + Fe^{4+}_{Sample} \rightarrow 2Fe^{3+}_{Solution} \quad (6)$$

$$Fe^{2+}_{Salt} + Co^{2+}_{Sample} \rightarrow Fe^{2+}_{Solution} + Co^{2+}_{Solution} \quad (7)$$

$$Fe^{2+}_{Salt} + Co^{3+}_{Sample} \rightarrow Fe^{3+}_{Solution} + Co^{2+}_{Solution} \quad (8)$$

$$2Fe^{2+}_{Salt} + Co^{4+}_{Sample} \rightarrow 2Fe^{3+}_{Solution} + Co^{2+}_{Solution} \quad (9)$$

Firstly, a flask with an acidic solution of HCl (preferably < 2M but adaptable to the solvability of the sample) is degassed under a flow of inert gas (Ar or N_2, at least 5.0 purity). Then a known amount of Fe^{2+} is added (in excess to the amount of high valent cations in the sample) in the form of a stable aqueous Fe^{2+} cation such as can be obtained from for example $(NH_4)_2Fe(SO_4)_2.6H_2O$ (i.e. "Mohr's salt"). This is allowed to dissolve before a fixed amount of sample is added to the solution. The solution with the salt and sample is kept under inert atmosphere until complete dissolution. Finally, before titration of the solution by a standardised solution of $Ce(SO_4)_2$, the redox indicator (Ferroin) and a few drops of concentrated phosphoric acid are added to the solution. The latter is added to prevent the unwanted precipitation of sulfates. During titration, the Ce^{4+} will react with the remaining M^{2+} cations (Co and Fe) in solutions to form Ce^{3+}, Co^{3+} and Fe^{3+}. At the equivalent point, the oxidation state of the B cations in the sample is given by (10).

$$x = \frac{MM^{(2+,3+)}.\left[\frac{M_{ms}}{MM_{ms}} - C_{Ce^{4+}}.V_{Ce^{4+}}\right]}{\left(n_{B,sample}.m_s - \frac{n_{B,sample}}{2}.MM_O.\left[\frac{M_{ms}}{MM_{ms}} - C_{Ce^{4+}}.V_{Ce^{4+}}\right]\right)} \quad (10)$$

In (10), $MM^{(2+,3+)}$ is a hypothetical molar mass of the compound where the Co and Fe would all be Co^{2+} and Fe^{3+} respectively, M_{ms} is the measured mass of the Fe^{2+} salt, MM_{ms} is the molecular mass of the Fe^{2+} salt, C_{Ce4+} and V_{Ce4+} are the concentration and volume of titrating solution used, $n_{B,sample}$ are the number of B sites in the hypothetical compound, m_s the weight of dissolved sample and MM_O the molar mass of the anion (note that when studying compounds with other anions, the coefficient ½ at the denominator might need to be corrected according to the anionic charge).

To exemplify this equation, on may consider the compound of anticipated formula Sr_2CoFeO_6. If the material were fully oxidised then the average oxidation state of the cations on the B site would be 4+. However, the molar mass $MM^{(2+,3+)}$ to be used in (10) would be that of the "hypothetical" composition "$Sr_2CoFeO_{4.5}$". The parameter "$n_{B,sample}$" would be 2. The value "x" obtained from (10) then needs to be added to the average oxidation state of the hypothetical compound $Sr_2CoFeO_{4.5}$. In this case the average oxidation state of the B site in the sample would then be $B^{2.5+x}$.

At this point several remarks should be made. If the sample dissolution in "dilute acid" is not feasible due to the speed of the reaction, Karen[191] suggested the use of concentrated acid in a sealed digestion cell. As an alternative to the use of a standardised solution of $Ce(SO_4)_2$.one might also consider the use of a standardized $KMnO_4$ solution. The advantage of the $KMnO_4$ route is the absence of the external indicator and the errors that this might bring if too concentrated. However, this is balanced by a loss of precision for a given titrating equipment set (each Mn will give five electrons instead of a single electron per reaction for which (10) needs additionally to be corrected).

For presentation in publications, cerimetric titration on certain RP3 samples were performed by Prof P. Karen using a procedure described in detail elsewhere.[192]

2.2.2 Physical methods.

2.2.2.1 Thermal methods.

Out of the available thermal methods, thermo-gravimetric analysis (T.G.A) was the method of choice for analysing the volatile content in precursors as well as the behaviour upon heating and subsequent cooling of the samples.

Measurements were performed either on Seiko SII TG/DTA thermal analyser and a Perkin Elmer TGA7 instruments in oxidising atmospheres (O_2), inert atmospheres (N_2) or reducing (5%-10% H_2 in Ar) atmospheres.

2.2.2.2 Diffraction techniques.

As the synthesised compounds were crystalline materials, diffraction techniques were essential to this work, both for basic as well as advanced characterisations. These are all based on the interaction between radiation and a periodic structure (See Fig. 17 (a)) that create constructive or destructive interferences according to "Bragg's Law" (11).

$$\lambda = 2.d.sin(\theta) \qquad (11)$$

λ being the radiation wavelength, d the inter-plane distance and θ the incidence angle with respect to the diffraction plane (cfr Fig. 17(a)).

For X-ray powder diffraction (XRD) and neutron powder diffraction (NPD), the intensity I_{hkl} of a reflection produced by a plane of miller indices hkl in a powder pattern depends on the structure factor F_{hkl} of the material. This is influenced by the nature of the atomic scatterers through their scattering factor f_j and their position (x,y,z) in the unit cell. (12) and (13)

$$I_{hkl} \propto |F_{hkl}|^2 \qquad (12)$$

$$F_{hkl} = \sum_{j=1}^{n} f_j . e^{2\pi i(hx+ky+lz)} \qquad (13)$$

The combination of equations (12) and (13) with equation (11) mean that diffraction patterns are unique for a given crystal structure and composition.

Factors affecting the diffracted intensities are the nature of the scatterers, their location as well as the symmetry of the studied materials. Therefore the information given by the techniques described hereafter each give their own complementary fingerprint allowing for a better understanding of a materials structure when pieced together.

2.2.2.3 XRD.

The fact that the wavelength of X-rays matches that of inter-atomic distances makes it an ideal tool to study its scattering, and ensuing diffraction pattern, that are created by crystalline materials. Consequently, XRD has become the "workhorse" for the investigation of crystalline materials. The technique can be used as a screening tool with conventional laboratory equipment (see hereunder 2.2.2.3.1) or as a more advanced tool for structure analysis and combined experiments at synchrotron sources (2.2.2.3.2). Experimental setups have been adapted for the study of powders, thin films and single crystals. However, only the first shall be described here.

2.2.2.3.1 Conventional.

The conventional laboratory powder X-ray diffractometers come in varying geometries and modes. Samples can be mounted on plates for use in reflection mode or, for transmission mode, on films or capillaries. Typically they use monochromatised $K_{\alpha 1}$ radiation from a Cu (λ=1.54060Å), Co (λ=1.78901Å), Cr (λ=2.28976Å) or Mo (λ=0.70932Å) X-ray source. The conventional X-ray diffractometers used for this study were equipped with either a Cu (for the Siemens D5000, Bruker D8 and Huber G670 diffractometers at UiO) or Co (for the Panalytical Xpert diffractometer at UoL). Cu tubes offer higher radiation flux though samples containing Fe or Co will have a higher background due to fluorescence. This can be somewhat diminished by using sources of different wavelengths (such as Co) or using modern detectors and software with built in energy filters. Of the four instruments used, three had the Bragg-Brentano configuration (Fig. 17(b)) mounted with a position sensitive detector. Patterns measured covered the $3°<2\theta<90°$ range and were used in reflection mode. The Huber G670 had the Guinier geometry (Fig 17 (c)) with a CCD camera detector that covered the $0°<\theta<100°$ range and was used in transmission mode.

XRD was the primary method for checking phase purity and completeness of the reactions on all samples.

2.2.2.3.2 (In-Situ) SRXRD.

When charged particles are accelerated in a magnetic field, they emit electromagnetic radiation. This property is used in synchrotron light sources where electrons are accelerated to great speeds. The wide spectrum of electromagnetic radiation obtained can then be used, either as a "white light source" or monochromated to desired wavelengths for the experiments. This flexibility as well as the high intensity has made synchrotron sources highly valued research tools for "Synchrotron Radiation X-ray Diffraction" (SRXRD) experiments. Their high intensity is synonymous with faster data collection permitting in-situ experiments. Whereas the wide spectrum of available wavelengths means that experiments can be performed in optimal conditions (i.e. with a reduction of parasitic effects such as absorption and fluorescence).

For this work, high resolution data from SRXRD experiments were collected at station 9.1 of the SRS (Daresbury – now decommissioned) and station ID31 of the ESRF (Grenoble). In-situ experiments were carried out at station BM01A of the Swiss-Norwegian beam line (ESRF) using a flat plate, 2D detector. The setup of the in situ experiments is shown in Fig 18.

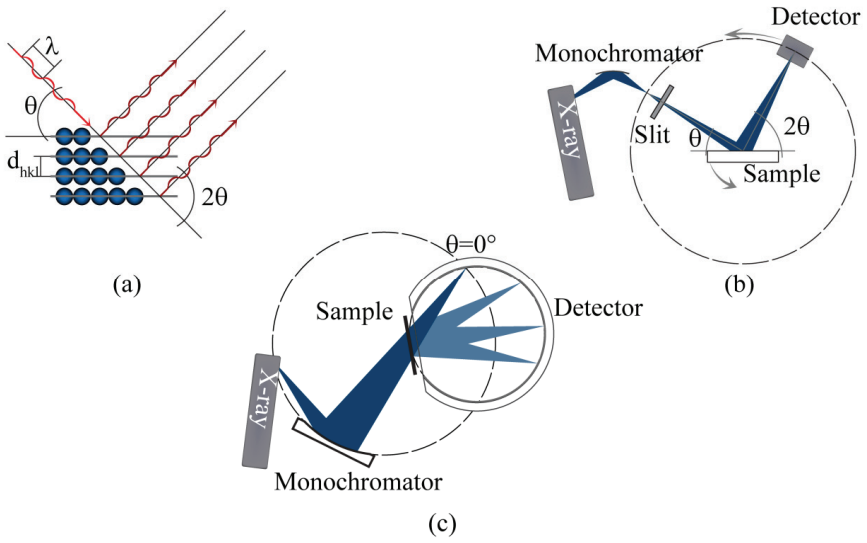

Fig 17. X-ray diffraction: principle and instrument geometries. (a) Diffraction of a monochromatic beam by a periodic structure. (b) The Bragg-Brentano instrument geometry in θ-2θ Reflection mode with coupled sample stage and detector. (c) The Guinier geometry (Transmission).

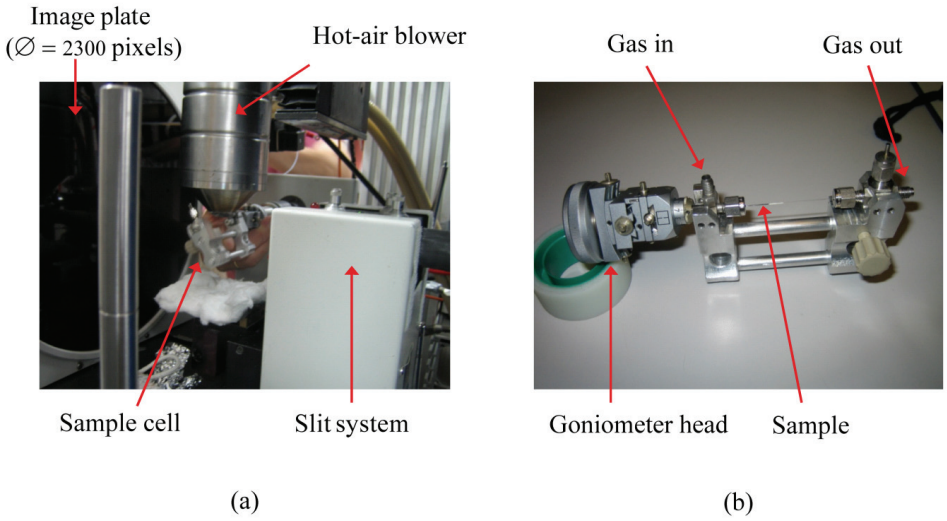

Fig 18. SNBL: Station BM01A: In-Situ powder diffraction. (a) Instrumental setup for in-situ experiments. (b) The powder Cell. (Photos courtesy of Dr R. Johnsen)

2.2.2.4 NPD.

As indicated by its name, Neutron Powder Diffraction (NPD) is the study of diffracted neutrons. Two methods can be used to obtain these neutrons: spallation and fission. In the first a target made from a heavy element is bombarded by a beam of high energy particles, usually protons, thus liberating a pulsed stream of neutrons. In the second, the neutrons are produced by the nuclear fission taking place in a reactor.

NPD offers some advantages over XRD. For example, the scattering factors depend neither on the incident angle of the beam, nor on the number of electrons surrounding the atom, also they are isotope specific. Hence, they offer good contrast between neighbouring elements and light elements are not outweighed by the heavier ones in the structure. Furthermore, neutrons posses a spin and can therefore interact with the magnetic moments of a material. However, like synchrotron radiation, it is a specialised technique requiring considerable resources for it to be functional. In addition to the aforementioned disadvantages and on the contrary to (SR)XRD, the samples need to "cool" after the experiment since upon exposure to neutrons they may become radioactive.

The NPD data collected over the course in this work were obtained from the PUS instrument at the JEEPII research reactor located at Kjeller (Norway). For more details on the instrument refer to Hauback *et al*.[193].

2.2.2.5 Phase identification and Structural analysis.

The collection of (SR)XRD, NPD and electron diffraction (ED) can all be used for (quantitative) phase identification in a multiphase sample and/or structural analysis of new phases.

Furthermore, given the possibility to calculate the intensity of diffraction peaks, it is possible to determine weight concentrations for each of the phases within a multiphase material.

The calculation of these intensities also forms the basis for the structural analysis of compounds through direct methods or refinement methods such as the Rietveld refinement.

In this latter method, a least squares technique is used to minimise the difference between the observed and calculated patterns for a crystal model by varying atomic parameters such as: site composition (i.e. the f_j's) and atomic coordinates (i.e. x, y and z). Some other parameters that affect the calculated intensities and that are taken into account in modern refinement software are the crystallographic domain size, anisotropies within the sample due to strain and stacking faults, displacement of the atoms around their average position (i.e. thermal

parameter) as well as the intrinsic broadening and asymmetries due to the diffractometer configuration used for collecting the data.

2.2.3 Spectroscopic techniques.

Complementary to diffraction techniques which give long range structural information, spectroscopic techniques allow the experimentalist to probe local effects such as compositional variations and nearest and next nearest neighbour interactions

2.2.3.1 EXAFS.

EXAFS or Extended X-ray Absorption Fine Structure is a spectroscopic technique similar to Electron Diffraction Spectroscopy (EDS), which is found on many modern electron microscopes, in so far as it probes the discrete energy levels of the inner shells of atoms. However instead of looking at the emission from these levels it looks at the absorption of the incoming radiation. During this process the electrons are excited from a low lying energy level to free state thus creating a photoelectron. Therefore not only is the energy absorption characteristic of an element, it is also influenced by the configuration of the electrons on the outer shells of the atom. This implies that the spectrum is influenced directly by the valence and coordination environment of the atom.

EXAFS experiments are usually performed at synchrotron facilities. The wavelength of the incident beam is varied so as to cover a range of energy levels around the absorption edge of the element of interest. The spectrum collected can then be treated in two different ways. The first looks at the position of the absorption edge relative to the metal and other standard materials. It makes up the XANES spectrum (X-ray Absorption Near Edge Structure) that is characteristic of the charge state of the cation. The second examines the spectrum after the absorption edge and constitutes the actual EXAFS spectrum. It is caused by interference between the ejected photo electron and the atoms surrounding the probed element. It therefore gives information on the nature, number and distance of these coordinating atoms.

Just as for diffraction techniques, EXAFS and XANES give information about the bulk of the material. However, they give only information on the local structure of the probed element thereby permitting studies on non- or poorly- crystalline materials. They also offer the possibility to look at the coordinating environment of selected elements.

For this work, Xanes plots were collected at station 7.1 of the SRS (Daresbury) and used to confirm the high oxidation states of Fe and Co in a selected RP3 compound.

2.2.3.2 Mössbauer spectroscopy.

2.2 Characterisation methods.

Mössbauer spectroscopy is a technique that probes the energetic states of an atoms nucleus. This is done by using high energy monochromatic γ radiation emitted by certain nuclei, such as ^{57}Fe. This is then absorbed by atoms possessing nuclear transition levels close to the emitted wavelength (e.g. in this case, Fe atoms). These energy levels are modified by the extra-nuclear electron density distribution mainly through the interaction with s electrons from the outer shells.

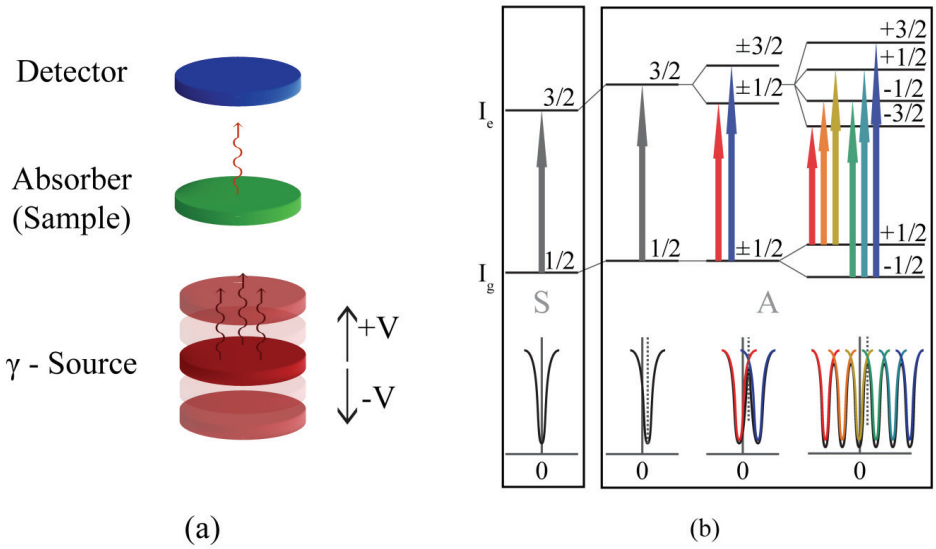

Fig 19. Mössbauer spectroscopy. (a) Experimental setup. (b) From left to right: "S" spectrum of the source, spectrum from the absorber "A", spectrum from the absorber with an internal electric field and spectrum from the absorber with a magnetic fields.

To probe the variation of these levels, modulation of the γ radiation is required. This can be achieved by moving the source or the target thereby creating a Doppler effect. The obtained spectra can then be characterised by (c.f. Fig 18.):[162, 194, 195]

- A chemical shift "δ" that gives the information on the charge state of the atom and its coordination environment.
- An electronic quadrupole splitting "Δ", that gives information on the presence (double peak) or absence (single peak) of an electric field surrounding the atom as well as its oxidation state. This is caused by the interaction of a non uniform electronic density at

the nucleus (i.e. spin number $I > ½$) with an anisotropic electronic environment surrounding the atom.

- A magnetic hyperfine splitting "H", when the nucleus is placed in a magnetic field. Thus giving information on the presence of a magnetic environment that is characterised by a sextuplet peak in the spectrum.

It should be noted that Mössbauer spectroscopy is dependent on the availability of appropriate γ-sources. Thereby meaning that only a limited number of elements can readily be measured, ^{57}Fe being one of the more common.

The Mössbauer data from this study was collected at the UoL by Dr M Thomas using a $^{57}Co/Rh$ source (25mCi). Therefore, only the environment of the Fe atoms in the examined RP3 structures have been probed.

2.2.3.3 Mass Spectroscopy.

Mass spectrometry was used in to analyse the gases (H_2, O_2 or CO_2) that might evolve from samples during the dissolution process of hydrated RP3 compounds by HCl (see section 3.4 of the following chapter). The mass spectrometer (MS) was connected to the exhaust of the reactor vessel and a constant flow of Ar was used as a carrier gas. Prior to the dissolution of the sample the method was validated by injection through a rubber septum of the acid in an empty chamber to check for dissolved gaseous species. Then by the injection of HCl over Zn chips to check the detection of evolving H_2.

The MS used was an "Omnistar GSD 301 O2" manufactured by Pfeiffer Vacuum mounted with an electron ionisation unit and a quadrupole analyser.

2.2.4 Magnetic properties.

2.2.4.1 Physical Property Measurement System.

The low temperature ($4°K<T<350°K$) magnetic properties of the RP3 compounds were measured using a "Physical Property Measuring System" (PPMS) from Quantum design. This instrument is based on a "Superconducting Quantum Interference Device" (SQUID) and measures minute changes in magnetic field. SQUIDs are coiled superconductors with one or two Josephson junctions (See Fig 20 (a)). The sample is moved through a coil of superconducting wire (pickup coil). These minute changes in field created by the samples displacements induce a current in the pickup coil. This current is then detected by the SQUID. Such systems allow to measure the dependencies of a sample's magnetisation, resistivity, heat capacity, thermal conductivities... as a function of temperature and/or magnetic field (fixed or varying). With these, one may calculate the susceptibilities, MR effects, Seebeck coefficients,

etc. Measurements performed for this work were: Magnetisation Vs Temperature (both in fixed and alternating fields), Magnetisation Vs Field and resistivities Vs Temperature.

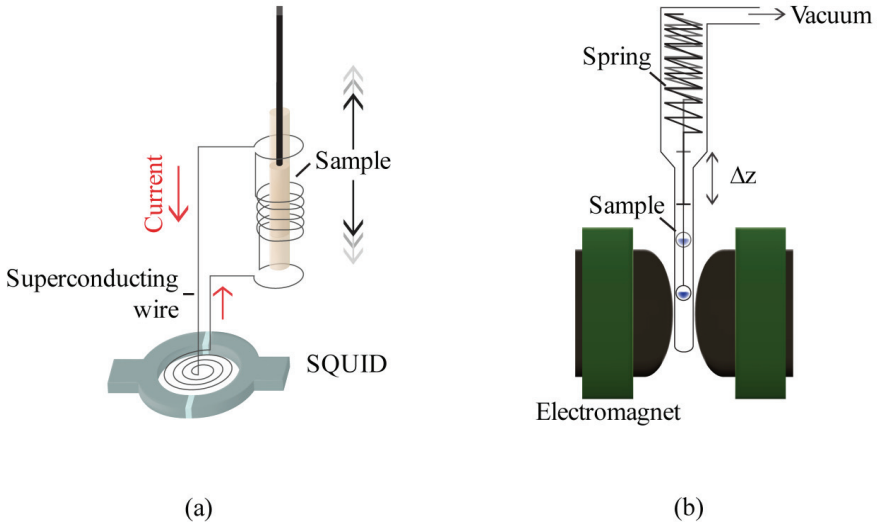

Fig 20. Schematic diagrams of a SQUID and a Faraday balance. (a) sample in a SQUID. (b) The Faraday- Balance.

2.2.4.2 Faraday Balance.

A Faraday balance at the University of Oslo was used for the high temperature magnetic susceptibility measurements of the RP3 ferrates (cfr Paper III). A cartoon of the experimental setup is represented in Fig. 20(b). It is comprised of a spring made from a diamagnetic material (a precision microbalance can also be used as an alternative) and an electromagnet with iron cores shaped as Faraday pole caps. Such cores create a field that obey (14) over sufficiently large heights.

$$H\frac{\partial H}{\partial z} = cst \qquad (14)$$

During a measurement, the sample is lowered between the iron cores in a quartz sample holder attached to the spring. A magnetic force is applied to the sample by the field created between the Faraday pole caps. The displacement along the vertical axis corresponding to a

new equilibrium between the spring's recoil and the magnetic force is then used to infer the susceptibility from equation (15). This has two unknowns: the sample's susceptibility and the product H.dH/dz. In order to determine the Field and its variation, the Faraday Balance was calibrated prior to use with $HgCo(SCN)_4$, a molecular paramagnet of known susceptibility. For High temperature measurements, a furnace was mounted between the iron cores and calibrated once more.

$$\chi . m . H \frac{\partial H}{\partial z} = -k\Delta z \qquad (15)$$

Where: k is the spring constant, m is the sample mass, Δz the vertical displacement, H the field generated by the electromagnet and dH/dz the Field gradient along the vertical axis.

3 Summary of results.

The work presented hereafter constitutes the summary of the results published, submitted or under review before their submission. Additional non published, but relevant results for the RP3 phases have also been included in this chapter. It focuses on the substitution and intercalation reactions that take place within the Ln-Sr-Fe-Co-O solid solutions and the effects of they have on the properties of the materials.

While many research groups have focused on perovskites, RP1, and RP2 phases, a much smaller community focused on the RP3 compounds. Amongst these a very small number have studied co-substituted RP3 ferrates. The most relevant published work for this study being $LaSr_3Fe_3O_{10}$ (Kuzushita *et al.*[196, 197]), $NdSr_3Fe_3O_9$ (Barrier *et al.*[97] and Pelloquin *et al.*[44]) and the $LaSr_3Fe_{1-x}M_xO_{10-d}$ system (M is one or more of Co, Al or Ga, studied by Armstrong *et al.*[198], Prado *et al.* [199] and Lee *et al.*[200, 201]). These studies independently treated certain aspects of the compounds such as magnetism, structure, hydration and ionic and electronic conduction properties either at high or low temperatures. The interest in this study lies within the fact that all these aspects are examined within one composition range.

3.1 Substituted RP3 structures: The $LnSr_3Fe_{1.5}Co_{1.5}O_{10}$ systems.

As the pure $LnSr_3Fe_3O_{10-\delta}$ compounds can be synthesised with Ln=La and Nd, the first part of the study looked into the substitution of La by other lanthanides in a high Co containing compounds using standard synthesis techniques. The aim being to test the effect the substitution of a smaller A^{3+} metal might have on the stability of $LaSr_3Co_{1.5}Fe_{1.5}O_{10}$ at room and elevated temperatures. The tested lanthanides were La, Pr,Gd, Yb, additionally, Y was also used. Many of the reported $Ln_4B_3O_{10}$ RP3 phases (B=Co or Ni)[202, 203] have used lanthanides from La through to Nd, suggesting that the structure tolerates substitution of at least the first four lanthanide elements. Furthermore the substitution of a smaller Fe cation should permit the insertion of smaller lanthanides in such compositions. This however could be compensated by the insertion of a bigger Sr cation in the case of the $LnSr_3M_3O_{10}$ compositions. For these compounds, assuming an ideal *I* 4/*m m m* structure and ionic radii provided by Shanon,[204] the tolerance factor would go down from c.a. 1 for Ln=La down to c.a. 0.9 for Ln=Ho.

Fig 21 shows the XRD diffraction patterns for Ln=La, Pr, Nd and Gd obtained through a solid state synthesis using oxides and carbonates as starting materials. Firing temperatures were

1000°C (12h) and 1350°C (three firings of 12h periods each with intermediate grindings). It also shows the identified phase types. Since the t factors involved are smaller than 1, orthorhombic distortions (with cell type $\sqrt{2}.a_p$, $\sqrt{2}.a_p$, $2.a_p$ for the RP∞ and $\sqrt{2}.a_p$, $\sqrt{2}.a_p$, c for higher order RP's) might occur for smaller lanthanides leading to new or split peaks that could possibly explain the unidentified peaks for Ln=Gd.

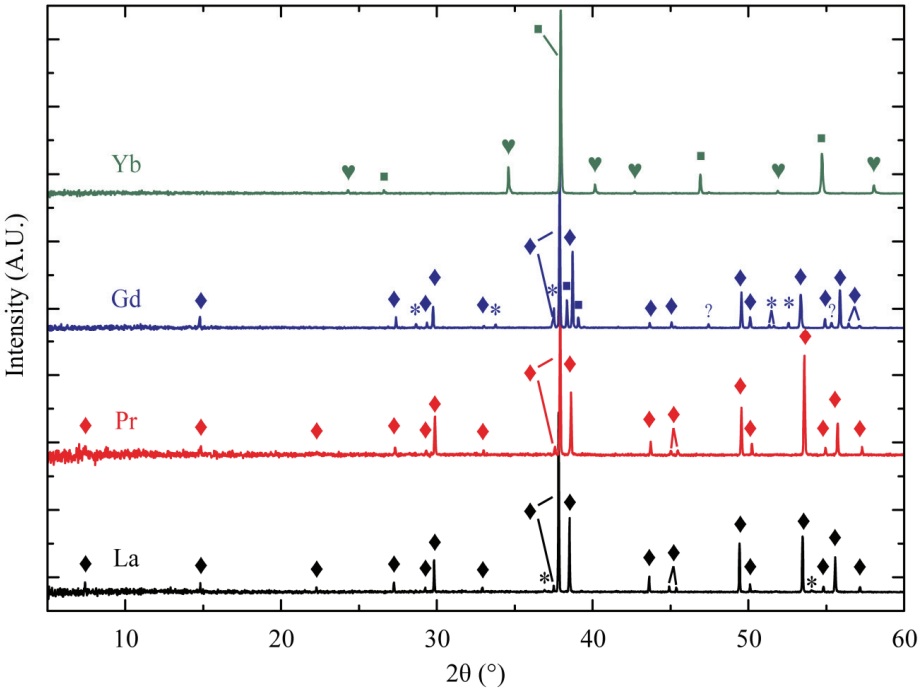

Fig. 21 XRD patterns of $LnSr_3Co_{1.5}Fe_{1.5}O_{10}$ compounds. Ln=La, Pr, Gd, Yb. Patterns were collected using monochromated Co Kα1 radiation. Phase attribution is as follows: ♦=RP3; ∗=RP1; ■=RP∞/ABX_3; ♥=Yb2O3; ? = unknown phase.

As can be seen from these patterns, using the conditions of air synthesis, the smaller lanthanides tend to favour mixes of lower RP phases. This was confirmed by TEM and EDS done on the Ln=Gd samples where a mixture between an ideal RP3 having the "*I*" symmetry and perovskite impurities were found. The presence of such phase mixture of RP phases is not unexpected as higher order RP phases have shown considerable amount of stacking faults with alternating lower members randomly packed.[205] Neither successive firings nor higher or lower firing temperatures improved the phase distribution. From these results, it would appear

that substitutions lanthanides should be bigger than Gd with the most promising new target material deemed to be Ln=Pr.

3.2 Oxygen vacancies in the $PrSr_3Fe_{1.5}Co_{1.5}O_{10}$ system.

The presence of the multivalent cations Fe and Co allow for the structural study of the compound as a function of annealing atmospheres. Indeed, cerimetric titrations and thermogravimetric analysis showed that the compound is stable from an average $B^{2.5+}$ oxidation state to a $B^{3.65+}$ (see Fig 22). These oxidation states were achieved by annealing in 10%H_2 in Ar (at 500°C) and O_2 (c.a. 300°C) respectively whereas the B^{3+} state is readily obtained by annealing at temperatures above 900°C in "inert" gases such as Ar or N_2 (purity > 5N). The high oxidation states of O_2 annealed samples have further been confirmed by XANES experiments (Fig 23) and Mössbauer spectra (See Table 1). As for $LaSr_3Fe_{1.5}Co_{1.5}O_{10}$ previously studied by Armstrong *et al.*[198], the structure adopts the ideal *I* 4/*m m m* structure of the RP3 compounds. The behaviour upon heating is stable and reversible for annealing in N_2 and O_2 at least up to 1200°. Above 500°C in H_2, the Fe^{3+} and Co^{2+} cations are reduced to metals thereby destroying the structure.

Table 1 Mössbauer parameters at 27°C and -196°C for samples treated in Oxygen at 300°C, Nitrogen at 1000°C and Hydrogen at 500°C. (Values relative to α-Fe)

Temperature	Annealing (Oxygen non stoichiometry – content.)	Chemical shift (mm.s-1)	Quadrupole splitting (mm.s-1)	Hyperfine Field (kOe)
27°C / 300K	O_2 ($\delta \approx 0.00 - O_{10}$)	0.10	0.24	0
	N_2 ($\delta \approx 1.00 - O_9$)	0.33/0.31	-0.46/1.06	432/0
	H_2 ($\delta \approx 1.75 - O_{8.25}$)	0.30	-0.043	220
-196°C / 77K	O_2 ($\delta \approx 0.00 - O_{10}$)	0.16/0.17/0.19	0.09/0-0.33/0.1	300/288/0
	N_2 ($\delta \approx 1.00 - O_9$)	0.43/0.45	-0.49/0.78	516/0
	H_2 ($\delta \approx 1.75 - O_{8.25}$)	0.43/0.25	-0.50/-0.27	511/466

From the Chemical shift column in Table 1 two observations can be made. Firstly, the Chemical Shift for the oxidised sample is smaller than that for the two reduced ones. Secondly, for both of the reduced phases, similar shifts are seen. Combined with the large Hyperfine Fields, one may deduce the presence of Fe^{4+} in the oxidised compound and Fe^{3+} in the reduced ones[195]. The presence of a Hyperfine Field further indicates the presence of an internal Magnetic field around the iron cations at 77K (i.e. -196°C), suggesting at least some short range magnetic order. More strikingly, the magnetic order is apparent even at high

temperatures for the N_2 annealed sample. Similarly, a broad feature in the H_2 annealed sample could be indicative of an emerging magnetic order. (See Fig 24).

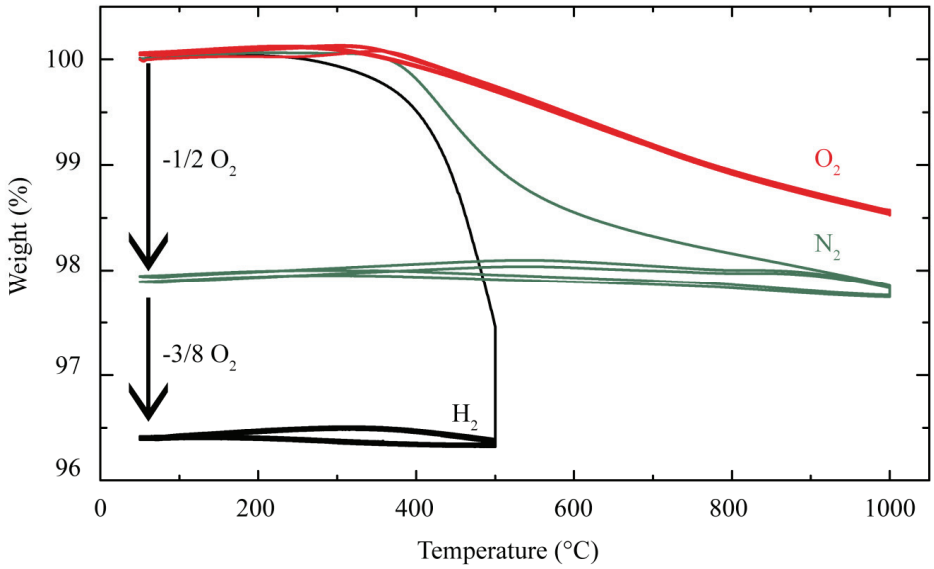

Fig. 22 Thermo gravimetric behaviour of $PrSr_3Co_{1.5}Fe_{1.5}O_{10-\delta}$ and stability upon cycling. In O_2, N_2 and H_2, Above 500°C in H_2 cycling is not stable.

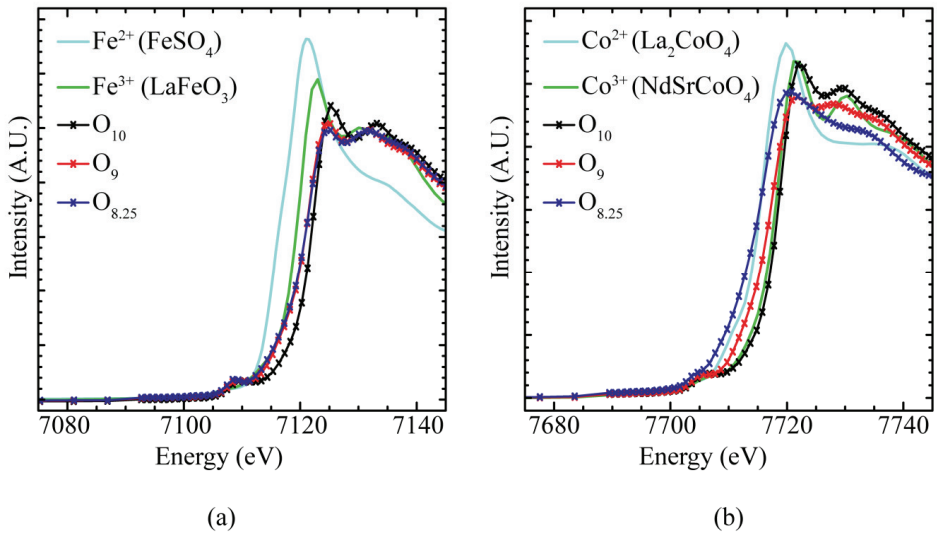

Fig. 23 Xanes plots of transition metal edges of $PrSr_3Co_{1.5}Fe_{1.5}O_{10-\delta}$. (a) Fe edge and (b) Co edge

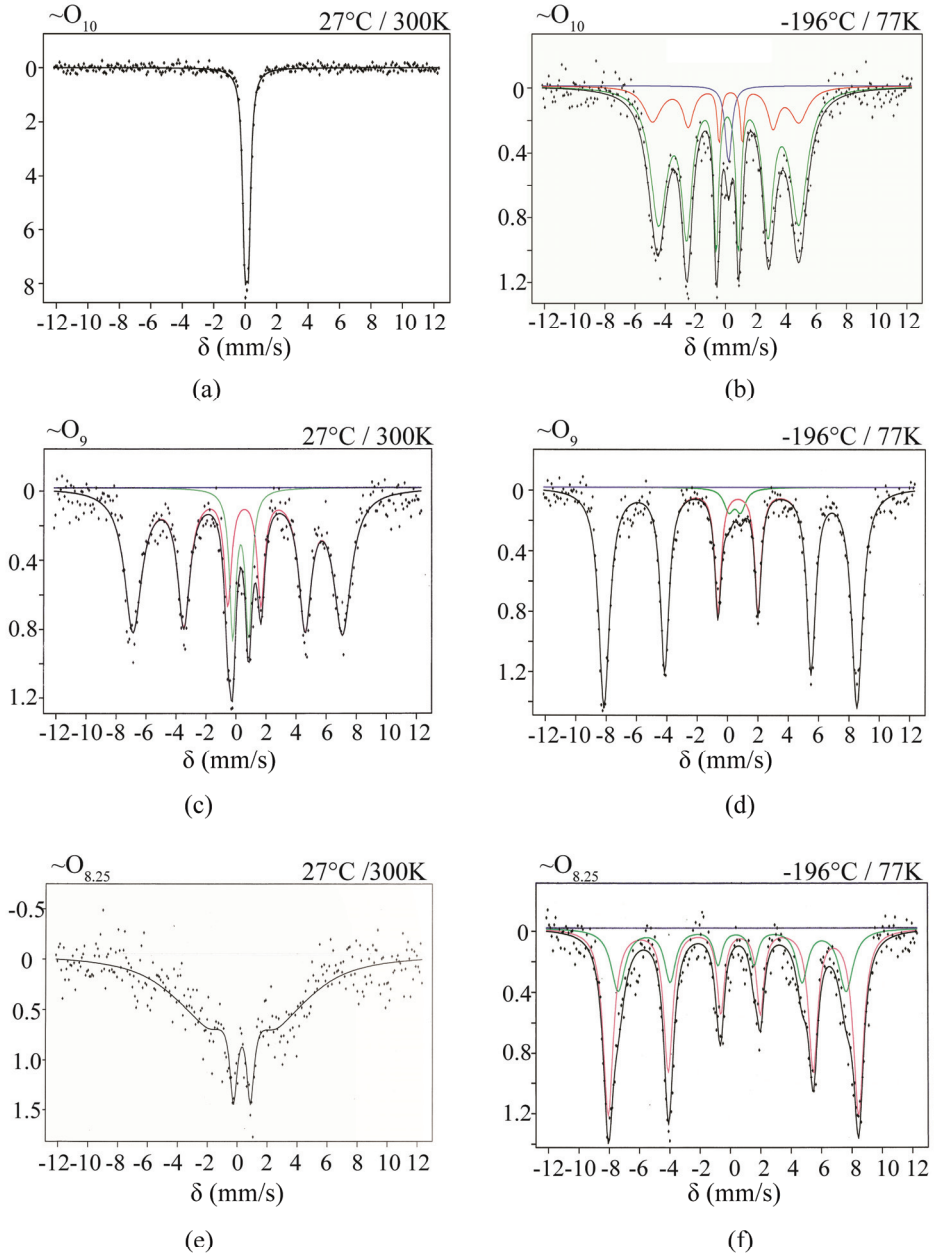

Fig. 24 Mössbauer spectra of oxygen deficient samples. (a) + (b) O_2 annealed - $PrSr_3Fe_{1.5}Co_{1.5}O_{\sim 10}$. (c) + (d) N_2 annealed – $PrSr_3Fe_{1.5}Co_{1.5}O_{\sim 9}$. (e) + (f) H_2 annealed $PrSr_3Fe_{1.5}Co_{1.5}O_{\sim 8.25}$.

Both the N_2 and H_2 annealed sample show a quadrupole splitting (doublet peak) at 300K that disappears at lower temperatures. Barrier *et al.* have studied the structure of the related $Sr_3NdFe_3O_9$.[97] The central perovskite blocks in this compound adopt a Brownmillerite like structure at room temperature where the tetrahedra constantly shift between two extreme configurations. Such shifting creates an uneven electronic distribution of the electronic density around the central Fe^{3+} cations.

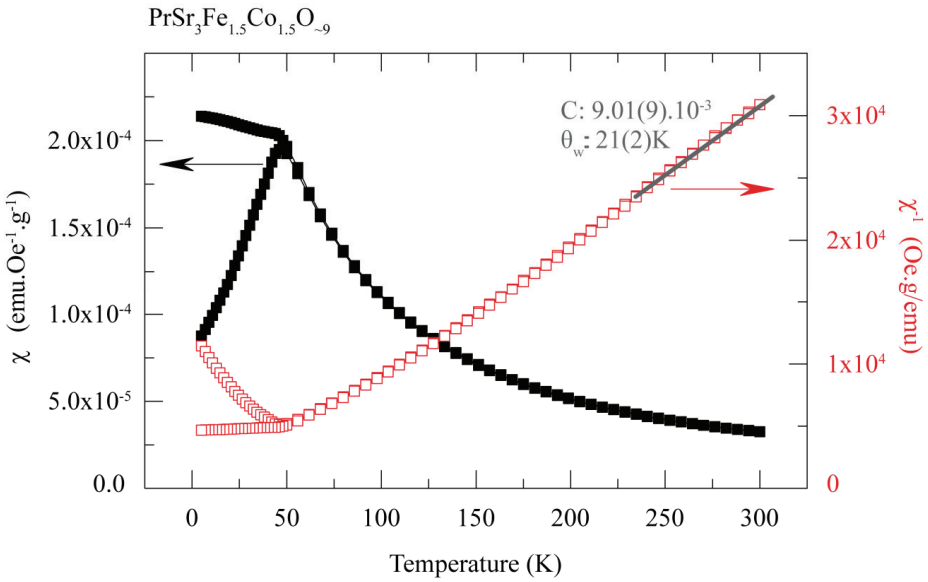

Fig 25. The magnetic susceptibility and its inverse vs temperature for $PrSr_3Fe_{1.5}Co_{1.5}O_9$

Susceptibility vs Temperature measurements were performed on the N_2 annealed sample with c.a. O_9 stoichiometry (Fig 25). This shows an AFM type ordering at low temperatures. A linear fit of the inverse susceptibility is possible and yields a positive value for θ_w and a Curie constant corresponding to a magnetic moment of c.a. $3.6\mu_b$ per B site. However, ascribing importance to these values would be erroneous as Mössbauer spectroscopy shows that magnetic order is still present at ambient pressures. Additional measurements at higher temperatures would therefore be needed to determine the transition temperature to the paramagnetic state. Furthermore, as the experiments were performed on two separately synthesised specimens, sample variability may also be a complicating factor.

Structural data at elevated temperatures was obtained from in situ variable temperature SRXRD studies (300K<T<1100K) of a fully oxidised sample (structure see Fig 26(a)).[206] These show a strong anisotropy in the character of the unit cell expansion with two successive regimes. The first characterised by a pure thermal expansion below 600 K and the second by a chemical expansion above 600 K (Fig 26 (b)). This effect is most noticeable on the evolution of the long axis of the structure (i.e. the **c** parameter). It was ascribed to the oxygen loss and creation of vacancies in the rock salt part of structure that then, through migration of oxygen atoms, lead to the concentration of the vacancies in the central perovskite layer.

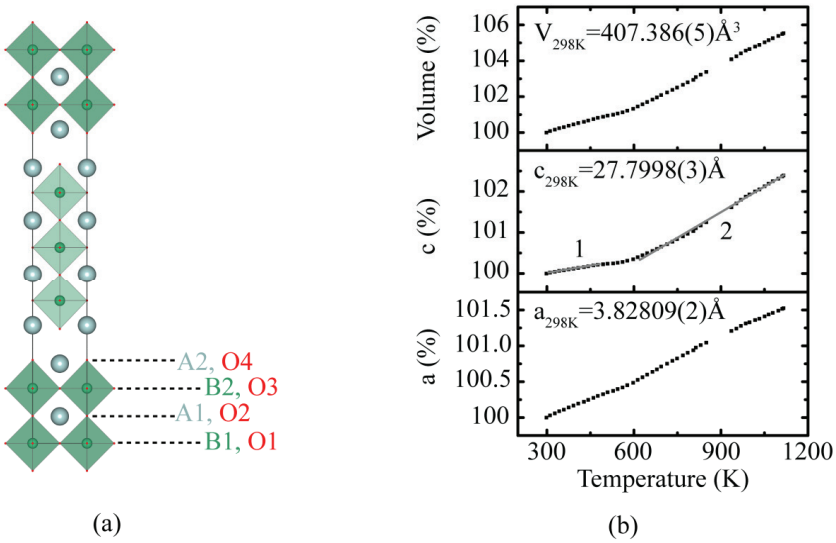

Fig 26. Structure and variation of the unit cell parameters of $PrSr_3Fe_{1.5}Co_{1.5}O_{10-d}$. (a) Structure and reference positions (b) Unit cell evolution vs temperature.

This process can be seen as the succession of the following steps:

- Vacancies are initially created in the more labile oxygen atoms of the rock salt layer (O4).
- These are then filled by the equatorial oxygen atoms (O3) bonded to the B2 site (outer perovskite blocks).
- In turn, apical oxygen atoms between the B1 and B2 sites fill these. (O2)
- Finally, the oxygen atoms that occupy the equatorial plane of the central perovskite block (O1) fill the vacancies present on the O2 site.

Though the structure retains the high symmetric structure at elevated temperatures, such a mechanism explains the formation of Brownmillerite/RP1 intergrowths, exemplified by $Sr_3NdFe_3O_9$, as well as the preferred occupation of the B site that is observed at room temperature. A distorted orthorhombic structure was also found for the $PrSr_3Fe_{1.5}Co_{1.5}O_9$ composition and it is expected to adopt the intergrowth structure though a full structure analysis has not been performed. Finally the onset of oxygen mobility at c.a. 600K corresponds also to the decline in electronic conductivity as observed by Armstrong *et al.* in $LaSr_3Co_{1.5}Fe_{1.5}O_{10-d}$. Given the similar behaviour of the $LnSr_3Co_{1.5}Fe_{1.5}O_{10-d}$ compounds such an effect is not unexpected since the creation of oxygen vacancies reduces the amount of conducting holes.

3.3 Hydration and Carbonatization in the $PrSr_3Fe_{1.5}Co_{1.5}O_{10-d}$ system.

Due to its similarity with $Sr_3NdFe_3O_9$ and other RP compounds, the title phase is prone to hydration. Several mechanisms were put forward such as reductive hydration in the case of $Sr_{2.5}La_{0.5}Co_{1.3}Ni_{0.7}(O,OH)_{7-y}$.[41] This conclusion was based on the change of the RP phase's $\mathbf{a}_p$ parameter that diminished upon hydration.

Several mechanisms can be used to explain the hydration of layered compounds for which a review article has been published.[39] In the specific case of the RP compounds, the subject is still open to debate as the hydration mechanism will affect the species present in the interlayer as well as dictate the evolution (or absence thereof) of gaseous species. For hydration experiments performed on $PrSr_3Fe_{1.5}Co_{1.5}O_9$ no significant changes in unit cell parameters were observed after topotactic insertion of water. However, there seem to be several prerequisites in order for topotactic insertions of gaseous species such as H_2O or CO_2 to take place[40]. Probably the most essential of these is the presence of oxygen vacancies (see See Fig 27(a)). This allows us to explain several current observations related to RP phases with similar compositions. Firstly, when the compound is fully oxidised, no spontaneous reaction with water is observed due to the absence of vacant sites. Secondly, depending on the ratio of lanthanide to alkaline earth present on the A-site, samples may be more or less prone to reaction as their acidities are tailored. Such observations can be explained if the reaction is partly driven by Acid-Base interactions in the compound. The reaction that fills oxygen vacancies with hydroxyl groups being accompanied by the insertion of stabilising water molecules within the rock-salt layers of the RP compounds. This reaction scheme is in real atmosphere subject to perturbations induced by the presence of carbon dioxide.

Indeed these oxides with their layered structure exhibit high basicity in certain structural segments, consequently showing a pronounced tendency to incorporate carbonate rather than hydroxyl anions. In particular at higher temperatures where hydroxyl forms are less stable and upon prolonged exposure to CO_2 containing atmospheres. This suggests that by selecting their oxygen stoichiometries, cationic composition and reaction conditions, RP-type oxides may be tuned to preferentially incorporate certain guest species.

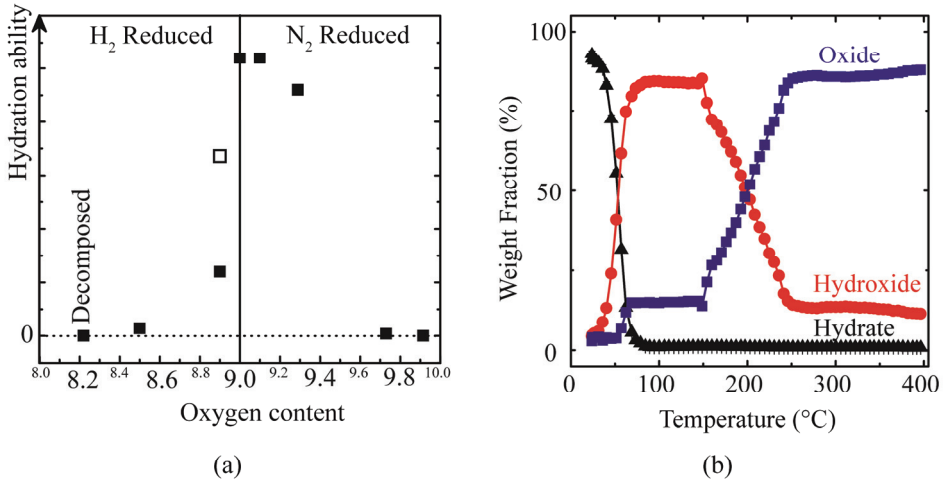

Fig 27. Characterisation of the topotactically hydrated $PrSr_3Fe_{1.5}Co_{1.5}O_9$. (a) Ability for hydration with respect to oxygen content. (b) Evolution of phase fractions upon heating as determined by SRXRD.

For the selective incorporation of hydroxide anions and molecular water, ambient temperatures and short reaction times were determined to be optimal. Upon heating a hydrated compound, loss of water and the conversion to an oxide hydroxide is established (Fig 27(b)) and was confirmed by thermogravimetric analyses. Given the weakness of metal-H_2O interactions, the decomposition of the hydrate into oxide hydroxide is more rapid than the opposite (acid - base) reaction. Additionally the intercalated water molecules distort the original tetragonal structure to form a monoclinic cell. Upon heating the monoclinic hydrate structure transforms to a primitive tetragonal oxide hydroxide structure, that finally reverse to the *I*-centered RP3 structure at high temperatures.[44] As shown in Fig. 28, the conversion from *I* (hydrate) to *P* (hydroxide) to *I* (HT phase) imposes repetitive shifting of the perovskite

layers from an eclipsed to a direct stacking of layers. The central perovskite block of the original RP phase can be seen as shifting to and fro by a vector (a, b, c) = (½, ½, 0). "c" being the long axis of the structure, i.e. parallel to the stacking direction of the ABX_3 layers.

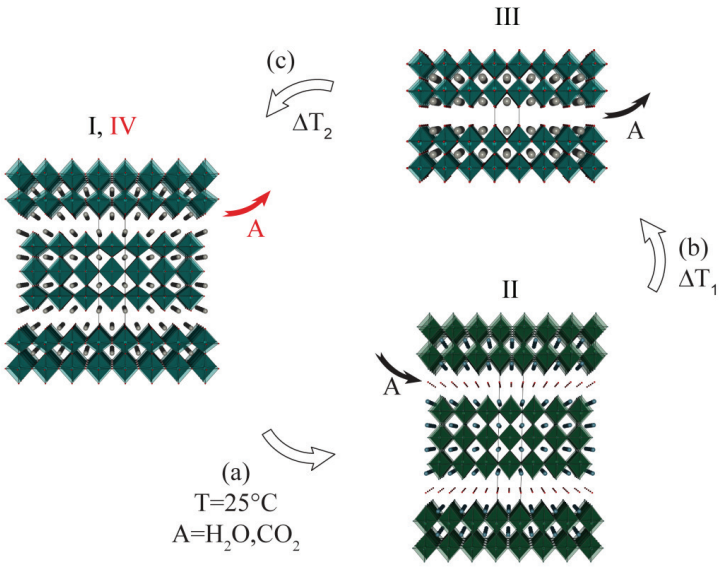

Fig 28 Topotactic deintercalation reactions of $PrSr_3Fe_{1.5}Co_{1.5}O_9$ system. (a) The reduced oxide "I" is exposed to "A" to form "II". (b) Upon heating of "II", "III" is formed via partial deintercallation of "A" located in the interlayer. (c) Further heating eliminates the remaining "A" from the apical/R.S. oxygen (i.e. the O4 site from Fig 25) from "III" to form "IV". Cooling of IV leads to "I".

Though many authors suppose at least a partial occupation by water of the (0, 0, ¼-ε) and (½, ½, ¼+ε) sites. [40, 44, 207-209] The matter is still debatable as other sites such as the tetrahedral (¼, ¼, z) could also accommodate water molecules. In an attempt to solve this issue, a reduced sample of composition $PrSr_3Fe_{1.5}Co_{1.5}O_9$ was prepared and hydrated over a water bath kept at room temperature. The sample was subsequently sent to station ID31 of the ESRF for High resolution X-ray powder diffraction. The wavelength used was 0.351450Å. The data was collected from 2θ=0.0005° to 35° using a step size of 0.0005°. The collected pattern (limited to 2θ<20°) is reproduced in Fig 29 (a). Attempts to fit it using the *I*12/*m*1 space group used previously proved unsuccessful. Upon careful examination of the data several additional features can be seen. Firstly in the region of corresponding to the ±1 0 9, 0 ±1 9 and 1, 1, 0 peaks of the "*I* 12/*m*1" space group, a broad background feature possibly due to triclinic

distortions can be seen (blue circle in Fig 29 (b)). Secondly, a clear splitting of certain $(0,0,l)_{hydrate}$ peaks can also be seen (Figs 29 (c)-(e), l=6, 10 and 18 respectively).

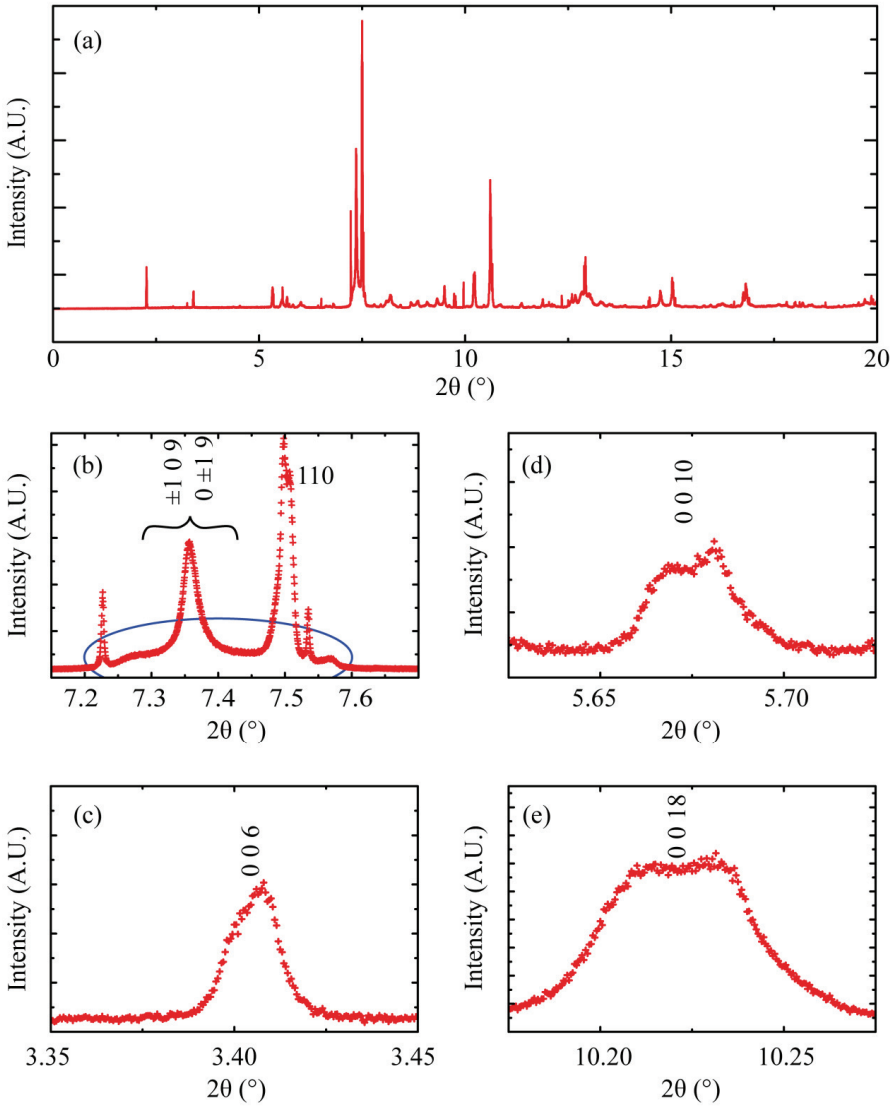

Fig 29. High resolution X-ray powder diffraction pattern of $PrSr_3Fe_{1.5}Co_{1.5}O_8(OH)_2.H_2O$. (a) Global pattern and (b) to (e) respectively enlargements of the ranges between 7.15°<2θ<7.7°, 3.35°<2θ<3.45° (0,0,6), 5.625°<2θ<5.725° (0, 0, 10) and 10.175°<2θ<10.275° (0, 0, 18). Pattern collected with λ = 0.351450Å

Plausible explanations for this are the presence of two phases or alternatively a change in cell dimension and/or symmetry caused by the intercalated water. Profile fitting was attempted both for a multiphase system and for larger cells/lower symmetry. However none of these proved satisfactory. To conclude the discussion of this HR-SRXRD study one also has to consider possible decomposition of the compound (either due to carbonation or due to the energetic beam) thereby adding to the complexity of analysing such a pattern.

3.4 The $PrSr_3(Fe_{1-x}Co_x)_3O_{10}$ solid solution (0.0≤x≤0.6).

It has already been mentioned in the introduction that Fe based perovskite compounds show interesting phenomenæ in the low temperature regimes. $SrFeO_3$ is a cubic AFM perovskite exhibiting metallic conduction down to low temperatures with a helical spin structure that has its axis along the $[111]_p$. The AFM order arises from the competition between local AFM interactions occurring through the M-O-M exchange and longer range FM interactions originating from the conducting electrons. $CaFeO_3$ on the other hand is an orthorhombic insulating perovskite with AFM. that exhibits CD. When studying the RP1 and RP2 strontium ferrates Dann *et al.* showed that both phases present AFM ordering.[210] The major difference between the two being that the RP2 is subject to CD whereas Mössbauer studies on the RP1 do not indicate any CD.[211]

In $SrFeO_3$, the A-site substitution of Sr by La induces CD. For x = 1/3, the disproportionated cations order within planes perpendicular to the $[1,1,1]_p$ direction. Their spins of the $Fe^{3+}$and Fe^{5+} align anti parallel to each other within these planes.[28, 212] Doping of the B-site by cobalt in the RP related ferrates induce FM interactions leading to competing interactions and the emergence of MR effects.[171, 213, 214]

The ideal *I4/mmm* tetragonal structure was determined by XRD. for the studied RP3 phases throughout the studied substitution range. [192] For the highest Co substitution, samples could only be synthesised at elevated temperatures (T_{max}: 1200°C) under flowing O_2. Fig 29 shows the evolution of the unit cell parameters as a function of Co substitution obtained from profile fitting of the powder XRD. data. Also represented in Fig. 30 are the oxygen contents as determined by cerimetric titration. Though the evolution of the basal plane ("a" parameter) is well described by a linear relation, the long axis ("c" parameter) and consequently the unit cell's volume expands non-linearly. This can be rationalised by two effects: Firstly the increase in oxygen vacancies as Co substitution increases the proportion of larger cations (i.e. with lower oxidation states). Secondly, for values of x greater than 1/3, there is a tendency to

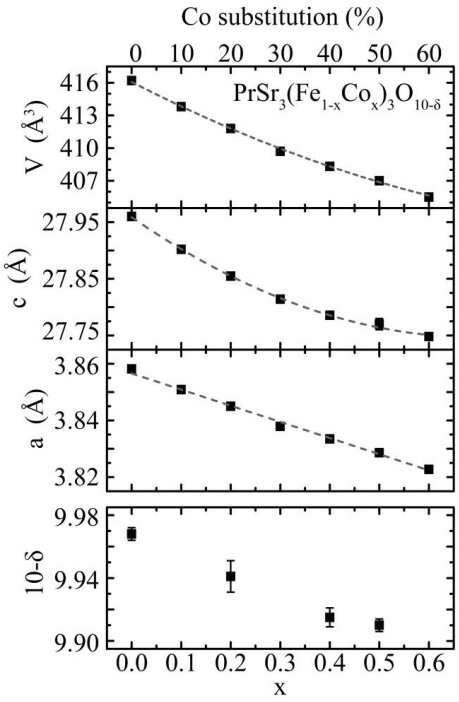

Fig 30. Unit cell parameters and oxygen content of the $PrSr_3(Fe_{1-x}Co_x)_3O_{10-\delta}$ solid solution under ambient conditions.

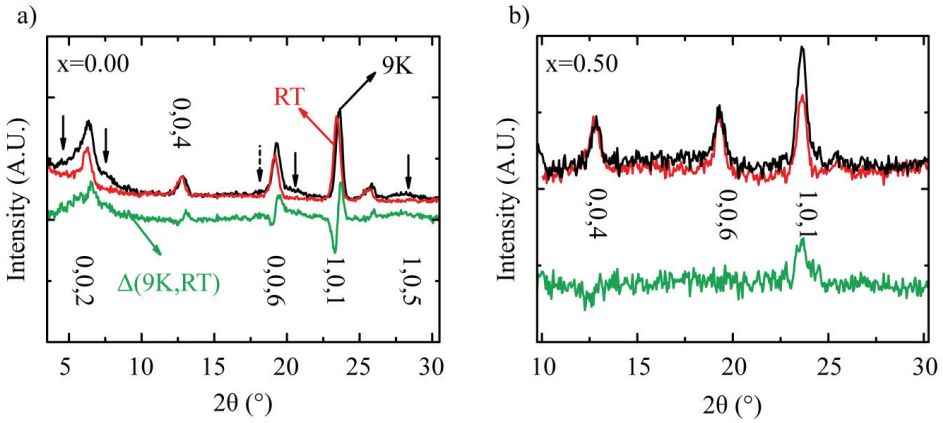

Fig 31. Low angle difference N.P.D. patterns. Room Temperature pattern (black), 9°K pattern (red) and difference pattern (green) for (a) x=0.00 and (b) x=0.50 with reflection indices.

replace the Fe^{4+} cation by Co^{4+} cations instead of the larger Co^{3+} as is suggested for substitution levels lower than 33%. Furthermore, deformation of the coordination polyhedra that lead to stabilisation of certain electronic configurations may also contribute to such effects. Neutron powder diffraction experiments performed on the x = 0.00 and x = 0.50 samples confirmed the high symmetry structure and high oxygen contents. In order to investigate the presence of long range magnetic ordering, data was also collected at 9K. Refining this data with the high symmetric structural model from room temperature gave reasonable fit statistics for the x=0.50 composition. In the case of the x=0.00 composition, using a similar refinement model resulted in bad refinement statistics. When comparing the room temperature and low temperature data for both compositions, only a small additional contribution to the "101" peak was found for x=0.50 (Fig 31 (b)). In the case of the parent compound, additional intensities can be seen for the "002", "006" and possibly even for the "105" peaks (Fig 31 (a)). The origin of this additional intensity can be explained either by small magnetic domain size or by a large magnetic supercell.

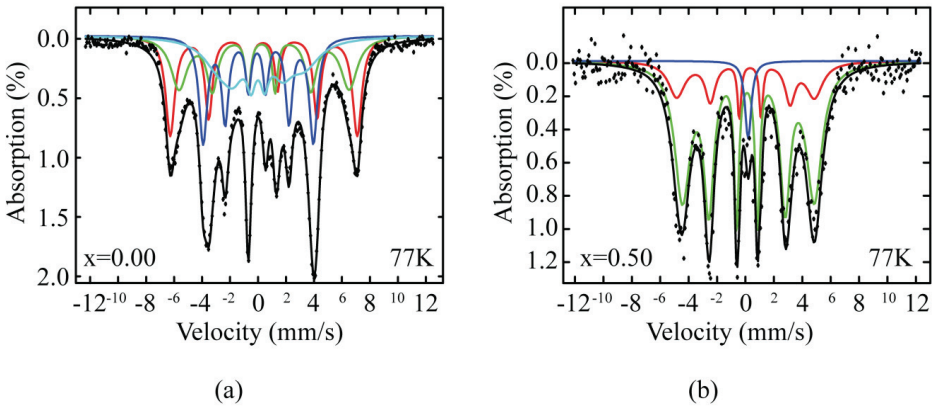

Fig 32 Low temperature Mössbauer spectra for $PrSr_3(Fe_{1-x}Co_x)_3O_{10-\delta}$. (a) x=0.00. (b) x=0.50

Mössbauer experiments performed on both compositions confirm the presence of a magnetic field in the vicinity of the iron cations for both compositions at 77K (Fig 32). The spectrum of the x=0.0 compound could be fitted by a partially charge disproportionated model (Fe^{3+}:Fe^{4+}:Fe^{5+} in a 2:1:1 ratio, see Table 2). For the $LaSr_3Fe_3O_{10}$ compound, Kuzushita *et al.* found similar results of a fully charge disproportionated state at low temperatures. Based on

their Mössbauer spectra, they suggested that the compound adopts a structure similar to $LaSr_2Fe_3O_9$ compound where the Fe^{3+} and Fe^{5+} order in planes perpendicular to the $[111]_p$.[196, 197] At 300K, both spectra show a single peak corresponding to an Fe^{4+} state.

Table 2. Mössbauer parameters of the low temperature spectra for x=0.0 and x=0.5 compositions.

	x=0.0 - 77K					x=0.5 - 77K			
	IS (mm/s)	Q (mm/s)	B_{HF} (kOe)	Rel. Area		IS (mm/s)	Q (mm/s)	B_{HF} (kOe)	Rel. Area
1 Fe^{3+}	0.377	0.060	414	1.06(6)	**1 Fe^{4+}**	0.171	-0.33(6)	300(5)	0.3
2 Fe^{3+}	0.344	0.175	377(2)	0.98(8)	**2 Fe^{4+}**	0.16(1)	0.09(4)	287(1)	1.0(5)
3 Fe^{5+}	-0.025	0.084	244.0	1	**3 Fe^{4+}**	0.19(3)	0.1	0	0.06(3)
4 Fe^{4+}	0.127	0.276	189(5)	1.0(1)					

For both compositions, the low temperature measurements are lower than the magnetic transition temperatures as evidenced by the low temperature magnetic susceptibility measurements (Fig 33). It should be noted that for x=0.0, the transition seems incomplete at 77K. This supports the hypotheses of incomplete disproportionation of the Fe^{4+} that was made previously in the text. Both low and high temperature magnetic susceptibility measurements were performed on all samples. The low temperature data shows the transition from an AFM behaviour to a FM dominated behaviour. Due to the high transition point for samples with higher Co content, "high temperature" measurements were carried out on a Faraday Balance. The data collected between 300K and 600K were used to perform a Curie-Weiss fit. The extracted Curie constant (C) and Weiss temperatures (θ_W) are given in Fig 34 (a) and the effective magnetic moments extracted from the Curie constant are represented in Fig 34 (b). The effective magnetic moments (μ_{eff}) are given per transition metal in the compound and have been corrected for the unpaired electrons of Pr^{3+}. As a small perovskite impurity was found in in the NPD data for the x=0.50 sample, a perovskite sample with similar cationic composition was synthesised and its susceptibility measured. Its susceptibility curve shows AFM type ordering and its C, θ_W and μ_{eff} parameters are represented by open symbols in Fig 34. The calculated values for μ_{eff} are consistent with a 3d4 configuration of Fe^{4+} (i.e. $\mu=4.9\mu_b$) for the parent compound. The lowering of the average μ_{eff} may be explained as follows: For Co contents smaller than 33%, the Co cations are inserted in the form of Co^{3+} low spin (i.e. $3d^6$, S=0 configuration). Once the doping exceeds 33%, the additional cobalt needs to be inserted in the form of Co^{4+}. For the x=0.50 sample a μ_{eff} value of 4 μ_b consistent with that

extracted from C can be achieved when considering spin only moments of Co^{3+}_{LS} (33.3%, S=0, $\mu_{Co3+}=0\mu_b$), Co^{4+}_{HS} (66.7%, S=2, $\mu_{Co4+}=4.9\mu_b$) and Fe^{4+}_{HS} (50%, S=2, $\mu_{Fe4+}=4.9\mu_b$). For the RP3 samples the deviations from the Curie – Weiss fit above 600K were attributed to the onset of oxygen mobility. However the $Co^{3+}_{LS} \rightarrow Co^{3+}_{HS}$ transition could also cause such deviations. The θ_W values are all positive and increase with Co substitution. This would indicate the presence of FM type interactions and, as aforementioned, is consistent with other reports of cobalt substituted ferrates.[171, 213, 214]

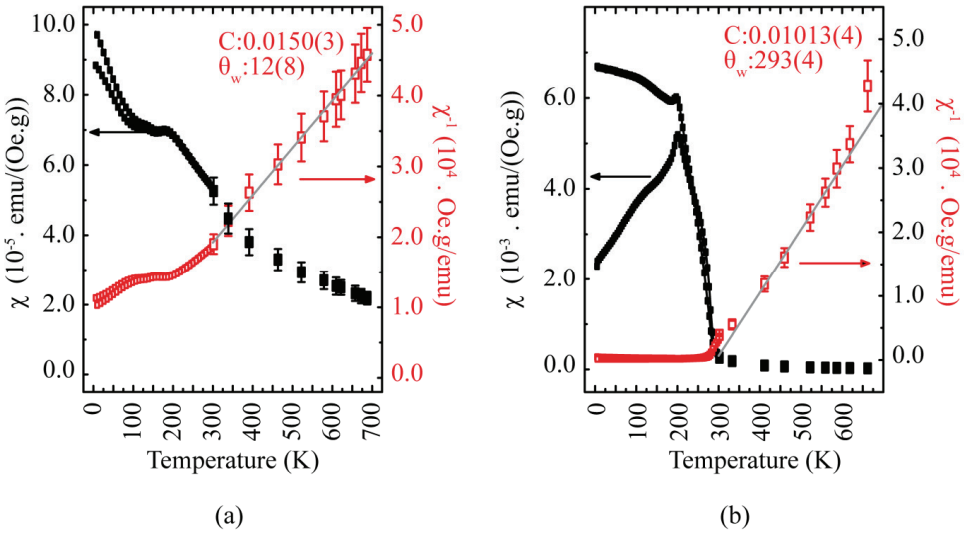

Fig 33. Magnetic susceptibility and its inverse at low and high temperatures. (a) For the unsubstituted compound. (b) For the 50% Co substituted compounds. Data was collected under fields of 20kOe (due to a weak signal) and 100Oe for x=0.00 and x=0.50 respectively.

The interaction between the AFM super exchange that occurs between two Fe^{4+} cations is therefore competing with FM interactions that occur through Co substitution leading to magnetic frustration within the structure. This has been verified by A.C. magnetisation measurements on samples with x=0.00, x=0.20 and x=0.50 compositions (Fig 35 (a), (b) and (c) respectively). While for the parent compound, the real and imaginary parts of the magnetisation are frequency independent, for the Co substituted samples they both show a frequency dependency. Of the three samples, the x=0.20 exhibits the strongest frequency dependency whereas the x=0.50 sample exhibits two features, the one occurring at lower

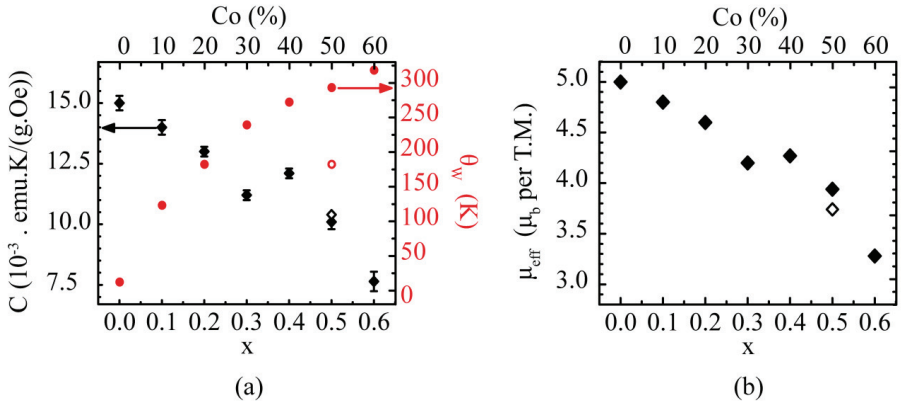

Fig 34. Curie-Weiss parameters and effective moment as a function of Co substitution levels. (a) C and θ_W values for RP3 phases (closed symbols) and the $Pr_{0.25}Sr_{0.75}Co_{0.5}Fe_{0.5}O_{3-\delta}$ perovskite (open symbols). (b) The effective magnetic moment extracted from the Curie constant for the RP3 (closed symbols) and the $Pr_{0.25}Sr_{0.75}Co_{0.5}Fe_{0.5}O_{3-\delta}$perovskite (open symbols).

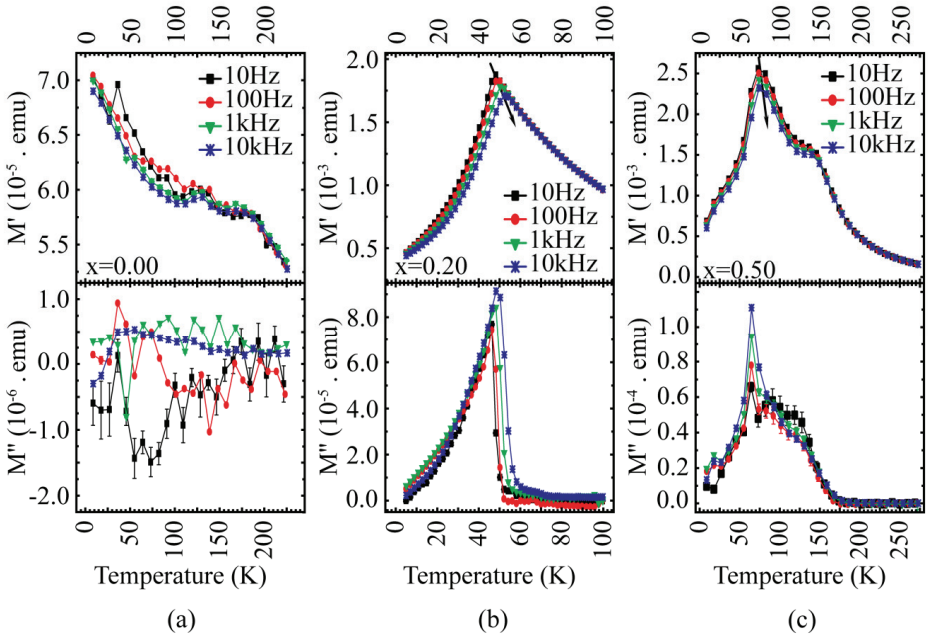

Fig 35. Real and Imaginary parts of frequency dependent magnetisation measurements vs temperature. (a) x=0.00, (b) x=0.20 and (c) x=0.50

temperatures being clearly frequency dependent. The presence of FM interactions is confirmed by the hystereses of the field dependent magnetisation at 5K for samples containing cobalt whereas for the parent compound none can be observed (See Fig 36.).

For the high Co containing samples, the M vs H curves collected at 5K present in addition a sudden increase in magnetisation at higher fields. This is characteristic either of clustered materials or of so-called meta-magnetic materials. The latter exhibit crossovers between different magnetic states of similar, but different, energies upon application of a critical field. For perovskite related phases, metamagnetism has been observed in RP2 ruthenates with itinerant electrons[215, 216] or insulators such as $DyBaCo_2O_{5.5+x}$ and $LaMn_{1-x}M_xO_3$ (M=Ga, Sc).[217, 218] Characteristic of these examples is the presence of a maximum in the temperature dependencies of the magnetic susceptibilities.

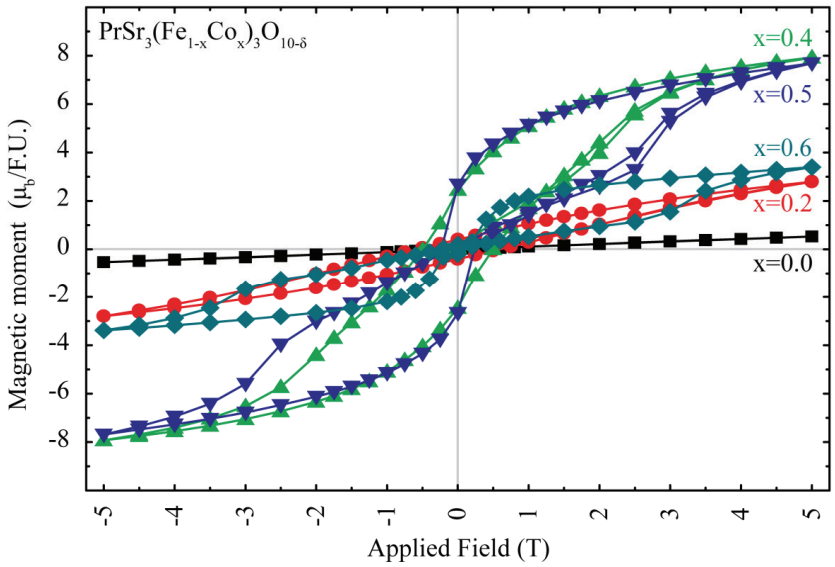

Fig 36. Field dependency of the magnetisation at 5K

In these samples, it is tempting to attribute the metamagnetic behaviour to the disruption of the AFM order by the insertion of the diamagnetic Co^{3+}_{LS} as occurs in the case of the $LaMn_{1-x}M_xO_3$ perovskite and may be one explanation. However the sudden increase of magnetisation is more visible for the higher Co contents where the electrons are more itinerant as is characterised by their decrease in resistivity observed upon Co doping (Fig 37). This

reduction of resistivity supports interaction models where increased FM interactions occur either through itinerant electrons (so called double exchange mechanism) or a $3d^5$-$3d^4$ (i.e. Co^{4+}_{HS} - Fe^{4+}_{HS}) superexchange mechanisms.

In effect it is hard to distinguish between a PM-FM metamagnetic model or a magnetic cluster model. As previously suggested,[192, 219] the cluster model supposes the presence of randomly oriented weak magnetic clusters. At low Co substitution levels, the non magnetic Co^{3+}_{LS} disrupt the AFM Fe^{4+}-O-Fe^{4+} interactions thereby creating AFM clusters. At higher substitution levels, the Co^{3+} would disrupt the Co^{4+}-O-Fe^{4+} magnetic interactions creating clusters of FM domains. At a critical value, these would then align with the excitation field, thus explaining the sudden jump in magnetisation observed for greater values of x.

Though the resistivities decrease monotonously with temperature for all samples, no model (i.e. polaron, VRH, Coulomb gap or Arrhenius) could successfully fit the low temperature resistivities. From a qualitative point of view, there seems to be an onset of a MI transition for the x=0.0 compound around 200K due to (partial) CO. This would be consistent both with the susceptibility data and with the Mössbauer data for the parent compound.

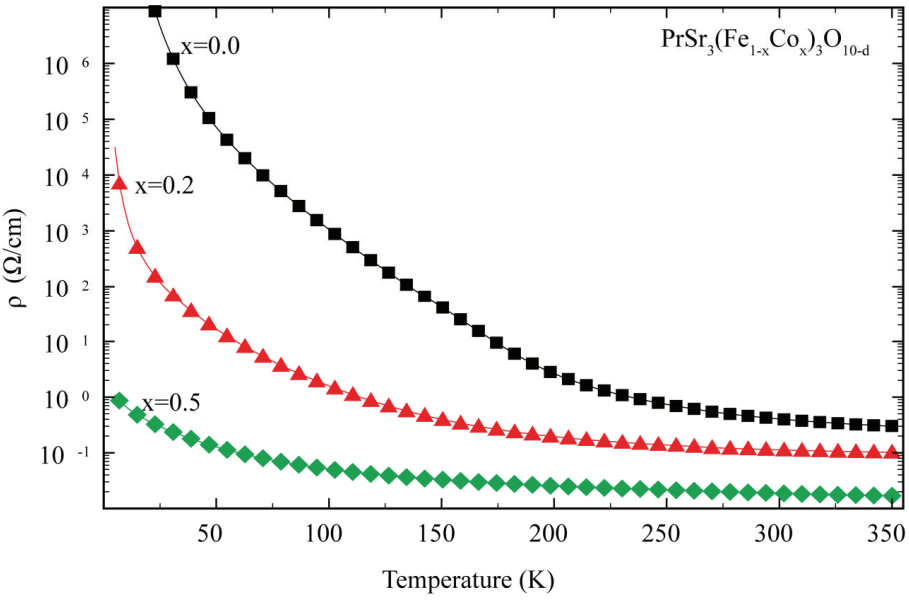

Fig 37 Resistivity as a function of composition and temperature in $PrSr_3(Fe_{1-x}Co_x)_3O_{10-\delta}$.

However, as shown by Akahoshi *et al.* the electric and magnetic properties of RP phases are highly anisotropic. [220] Indeed, upon Co substitution of Fe in $Sr_3Fe_2O_7$, magnetisation and

resistivities vary widely between in plane (i.e. with field or current flow parallel to the rock salt layers) and out of plane (i.e. field and current flow parallel to the long axis "c") measurements. For high Co content a near metallic conductivity is even observed in plane whereas a semi conductive like resistivity is observed for the out of plane resistivity. The mixing of these anisotropic properties in polycrystalline samples with, in addition, effects such as non negligible tunnelling between adjacent perovskite blocks or grain effects, renders the attribution of a dominating conducting mechanism difficult at best.

4 Perspectives

In the introduction, much focus was set on the versatility of the ABX_3 compounds both from a structural as well as from the application point of view. The current work, revolved around the RP3 compounds within the $PrSr_3(Fe_{1-x}Co_x)_3O_{10-\delta}$ and the behaviour of the x=0.5 compound in different atmospheres. This led to various interesting results such as amongst other things the insertion of water in mixed B-site RP3 compounds, rationalising intergrowths between Brownmillerite and RP1 and their derivation from RP3 compounds as well as the low temperature properties of the aforementioned solid solution. These are all aspects that are of interest in technological applications such as catalysis or micro-electronics. Based on this work and the scarceness of available publications on mixed RPn systems in general and RP3's in particular, further extension of this work opens an exponential amount of possibilities. These may be divided into three heavily interconnected categories: Composition, Properties and Superstructures.

From the compositional point of view, several aspects might be studied. Firstly tuning the synthesis conditions in order to obtain other members of the $(Pr_{¼}Sr_{¾})_{n+1}(Fe_{1-x}Co_x)_nO_{(3n+1)-\delta}$ system. Thereafter one might consider, within each RPn system, investigating various synthesis conditions and methods for studying the A site substitution. Aiming either at inserting smaller lanthanides, using different elements (e.g. Ca, Ba, Y,...) or changing the ratio between the two. Such a parametric study on the A site composition would allow examining properties such as proton and oxide ion conduction, catalytic properties or host-guest substitutions and intercalations. All of which could be obtained by tuning the acidity/basicity and redox properties of the compound.

Similarly, one might consider studying the effect of the B site composition on the structure of the compounds. In particular, studying the electronic transitions upon doping and substitutions of the Fe sublattice would be of particular interest. Indeed, for the $AFeO_3$ system, substituting the B site with 10% or less has shown drastic effects for the conductivities of the samples. Understanding the effects of small substitution levels on the electronic and magnetic transitions that take place in various RP ferrate systems would provide a general understanding of such 2D systems and the tuning of their electronic structure ("band gap engineering"). Again, one might also consider changing Co for another magnetic element such as Mn that might induce J-T type distortions or other CD/CO effects. Other magnetic atoms of interest for Fe (co-)substitution might be V, Cr or Ni. Of equal importance to the electronic and magnetic properties would involve substitution of Fe by non magnetic cations,

either multi-valent such as Ti or Cu or single valent atoms for example Al. The latter was shown to favour the formation of oxygen vacancies in the central perovskite block that force the electron holes to localise in the outer perovskite block.[221] In conjunction with A site doping, one may also consider targeting specific compositions where one might obtain atomic, charge and/or orbital ordering phenomena. The last compositional variable that can be considered would be the anion. Examining either the effects of deficiencies (both at high and low temperatures), or even substitution of the lattice oxygen by other chalcogenides, pnictides or halogenides. Such substitutions would heavily influence the overlap between the anionic and cationic orbitals and hence the materials properties.

As an alternative to classical wet and dry chemical synthesis methods, using thin film techniques to investigate specific superstructures would prove valuable from the chemical and application point of view. For example, such methods would be ideally suited for creating superstructures with alternating Co and Fe perovskite blocks or even creating ordered structures with alternating Fe and other transition metals within a given perovskite layer. These could be interesting for the creation of spintronic components. Thin film techniques would also be well suited to create epitaxial films for studying the anisotropy of the magnetic, electronic and ionic properties. Such studies have already shown that alternation of two different perovskite layers can cause interesting phenomena in their own right (e.g 2D electron gases in SrTiO3/LaAlO3 superstructures[222]). Ideally the studies on thin films would need to be conducted in conjunction with the growth of macroscopic single crystals so as to minimise/investigate the effects of nanoscale versus bulk. Using low temperature thin film techniques such as atomic layer deposition would in addition permit the study of crystallinity on the compound's properties.

Finally studying the intercalation chemistry of the RPn phases opens up a whole field of research possibilities for creating novel catalysts and hybrid materials for electronic applications. Understanding the precise driving force of the hydration and carbonation mechanisms through in situ studies with collection of high resolution X-ray and Neutron powder data (i.e. diffraction and absorption) in perfectly controlled atmospheres (p_{O_2}, p_{H_2O} and p_{CO_2}) would provide a significant stepping stone for the creation of novel intercalated materials. Furthermore, creating novel intercalated hybrid materials would permit the creation of highly dimensional electronic structures through variations of the intercalated ligand.

5 Publication list and author's own contribution.

Paper I: Temperature dependant X-ray diffraction study of $PrSr_3Co_{1.5}Fe_{1.5}O_{10-\delta}$; n= 3 Ruddlesden-Popper phase. L. Jantsky, P. Norby, M.J. Rosseinsky and H. Fjellvåg, *Zeitschrift für Kristallographie*, 2009, **224**, p295-p301

The author contributed to the manuscript through the synthesis, data collection (with P.N. at SNBL), data analysis and active participation in the writing of manuscript.

Paper II: Tuning of water and hydroxide content of intercalated Ruddlesden-Popper type oxides in the $PrSr_3Co_{1.5}Fe_{1.5}O_{10-\delta}$ system. L. Jantsky, A. Demont, H. Okamoto and H. Fjellvåg. *Inorganic Chemistry* (Submitted).

The author contributed to the manuscript through the synthesis of compounds, forced hydration, analysis of conventional and in situ SRXRD data and active participation in the writing of manuscript Primary XRD analysis of hydrated phase and some sample preparation were performed in collaboration with Dr A. Demont.

Paper III: Investigating the magnetic interactions in $PrSr_3(Fe_{1-x}Co_x)_3O_{10-\delta}$, a solid solution in an n=3 Ruddlesden-Popper material. L. Jantsky, H. Okamoto, M.F. Thomas, P. Karen, M.J. Rosseinsky and H. Fjellvåg. (Manuscript to be submitted)

The author contributed to the manuscript through sample synthesis, analysis of XRD and PND data, analysis of data from magnetic measurement, and participation in the writing of the manuscript.

6 References

1. G. Rose, *Poggendorffs Annalen der Physik und Chemie*, 1839, **XXXXVIII**, 558-560.
2. H. D. Megaw, *Proceedings of the Physical Society*, 1946, **58**, 133-152.
3. S. Roberts, *Physical Review*, 1947, **71**, 890.
4. D. F. Rushman and M. A. Strivens, *Transactions of the Faraday Society*, 1946, **42**, A231-A238.
5. B. Matthias and A. von Hippel, *Physical Review*, 1948, **73**, 1378.
6. J. M. Moreau, C. Michel, R. Gerson and W. J. James, *Journal of Physics and Chemistry of Solids*, 1971, **32**, 1315-1320.
7. R. H. Mitchell, *Perovskites: modern and ancient*, Almaz Press, Thunder Bay, Ont., 2002.
8. V. Goldschmidt, *Naturwissenschaften*, 1926.
9. T. Takeda, Y. Yamaguchi and H. Watanabe, *Journal of the Physical Society of Japan*, 1972, **33**, 967-969.
10. T. Takeda, R. Kanno, Y. Kawamoto, M. Takano, S. Kawasaki, T. Kamiyama and F. Izumi, *Solid State Sciences*, 2000, **2**, 673-687.
11. P. M. Woodward, D. E. Cox, E. Moshopoulou, A. W. Sleight and S. Morimoto, *Physical Review B*, 2000, **62**, 844-855.
12. I. G. De Muro, M. Insausti, L. Lezama and T. Rojo, *Journal of Solid State Chemistry*, 2005, **178**, 1712-1719.
13. A. Glazer, *Crystal Physics*, 1975.
14. J. B. Goodenough, *Reports on Progress in Physics*, 2004, **67**, 1915.
15. Y. W. Long, N. Hayashi, T. Saito, M. Azuma, S. Muranaka and Y. Shimakawa, *Nature*, 2009, **458**, 60-63.
16. Y. Shimakawa, *Inorganic Chemistry*, 2008, **47**, 8562-8570.
17. A. Prodi, E. Gilioli, A. Gauzzi, F. Licci, M. Marezio, F. Bolzoni, Q. Huang, A. Santoro and J. W. Lynn, *Nature Materials*, 2004, **3**, 48-52.
18. T. Nakajima, H. Kageyama, M. Ichihara, K. Ohoyama, H. Yoshizawa and Y. Ueda, *Journal of Solid State Chemistry*, 2004, **177**, 987-999.
19. T. Nakajima, H. Kageyama, H. Yoshizawa and Y. Ueda, *Journal of the Physical Society of Japan*, 2002, **71**, 2843.
20. S. Nakamura, M. Tanaka, H. Kato and Y. Tokura, *Journal of the Physical Society of Japan*, 2003, **72**, 424-428.
21. E. E. Rodriguez, T. Proffen, A. Llobet, J. J. Rhyne and J. F. Mitchell, *Physical Review B - Condensed Matter and Materials Physics*, 2005, **71**, 1-9.
22. Y. Tsujimoto, C. Tassel, N. Hayashi and T. Watanabe, *Nature*, 2007.
23. J. P. Hodges, S. Short, J. D. Jorgensen, X. Xiong, B. Dabrowski, S. M. Mini and C. W. Kimball, *Journal of Solid State Chemistry*, 2000, **151**, 190-209.
24. J. Nakamura, M. Karppinen, P. Karen, J. Lindén and H. Yamauchi, *Physical Review B*, 2004, **70**, 144104.
25. P. Karen and P. M. Woodward, *Journal of Materials Chemistry*, 1999, **9**, 789-797.
26. P. Karen, *Journal of Solid State Chemistry*, 2003.
27. F. Millange, V. Caignaert, B. Domengès, B. Raveau and E. Suard, *Chemistry of Materials*, 1998, **10**, 1974-1983.
28. P. D. Battle, T. C. Gibb and P. Lightfoot, *Journal of Solid State Chemistry*, 1990, **84**, 271-279.
29. B. C. Tofield and W. R. Scott, *Journal of Solid State Chemistry*, 1974, **10**, 183-194.

30. Q. Huang, V. Lynn Karen, A. Santoro, A. Kjekshus and e. al., *Journal of Solid State Chemistry*, 2003.
31. J. Hadermann, A. M. Abakumov, J. J. Adkin and M. A. Hayward, *Journal of the American Chemical Society*, 2009, **131**, 10598-10604.
32. A. V. Powell and P. D. Battle, *Journal of Alloys and Compounds*, 1996, **232**, 147-153.
33. S. V. Krivovichev, *Zeitschrift für Kristallographie*, 2008, **223**, 109-113.
34. A. Velden and M. Jansen, *Zeitschrift für anorganische und allgemeine Chemie*, 2004, **630**, 234-238.
35. K. Meisel, *Zeitschrift für anorganische und allgemeine Chemie*, 1932, **207**, 121-128.
36. H. Braekken, *Zeitschrift für Kristallographie*, 1931, **78**, 485.
37. D. B. Mitzi, *Journal of the Chemical Society, Dalton Transactions*, 2001, 1-12.
38. C. A. Bremner, M. Simpson and W. T. A. Harrison, *Journal of the American Chemical Society*, 2002, **124**, 10960-10961.
39. K. G. Sanjaya Ranmohotti, E. Josepha, J. Choi, J. Zhang and J. B. Wiley, *Advanced Materials*, 2011, **23**, 442-460.
40. L. Jantsky, A. Demont, H. Okamoto and H. Fjellvåg, *Submitted to Inorganic chemistry*, 2012.
41. Y. Bréard, B. Raveau, D. Pelloquin and A. Maignan, *Journal of Materials Chemistry*, 2007, **17**, 2818-2823.
42. D. Pelloquin, N. Barrier, D. Flahaut, V. Caignaert and A. Maignan, *Chemistry of Materials*, 2005, **17**, 773-780.
43. D. Pelloquin, N. Barrier, A. Maignan and V. Caignaert, *Solid State Sciences*, 2005.
44. D. Pelloquin, J. Hadermann, M. Giot and V. Caignaert, *Chemistry of Materials*, 2004, **16**, 1715-1723.
45. B. Aurivillius, *Arkiv För Kemi*, 1949, **1**, 463.
46. B. Aurivillius, *Arkiv Fur Kemi*, 1949, **1**, 499.
47. B. Aurivillius, *Arkiv För Kemi*, 1950, **2**, 519.
48. M. Dion, M. Ganne and M. Tournoux, *Materials Research Bulletin*, 1981, **16**, 1429-1435.
49. A. J. Jacobson, J. W. Johnson and J. T. Lewandowski, *Inorganic Chemistry*, 1985, **24**, 3727-3729.
50. S. N. Ruddlesden and P. Popper, *Acta Crystallographica*, 1957, **10**, 538-539.
51. S. N. Ruddlesden and P. Popper, *Acta Crystallographica*, 1958, **11**, 55.
52. M. Dion, M. Ganne and M. Tournoux, *Français*, 1984, **21**, 92-103.
53. S. N. Ruddlesden and P. Popper, *Acta Crystallographica*, 1958, **11**, 54-55.
54. K. R. Kendall, C. Navas, J. K. Thomas and H. C. Zur Loye, *Chemistry of Materials*, 1996, **8**, 642-649.
55. M. Mazurek, A. Lisińska-Czekaj, Z. Surowiec, E. Jartych and D. Czekaj, *Acta Physica Polonica A*, 2011, **119**, 72-74.
56. G. N. Subbanna, T. N. G. Row and C. N. R. Rao, *Journal of Solid State Chemistry*, 1990, **86**, 206-211.
57. Ismunandar, B. A. Hunter and B. J. Kennedy, *Solid State Ionics*, 1998, **112**, 281-289.
58. B. J. Kennedy, Q. Zhou, Ismunandar, Y. Kubota and K. Kato, *Journal of Solid State Chemistry*, 2008, **181**, 1377-1386.
59. A. Snedden, K. S. Knight and P. Lightfoot, *Journal of Solid State Chemistry*, 2003, **173**, 309-313.
60. F. Lichtenberg, A. Herrnberger and K. Wiedenmann, *Progress in Solid State Chemistry*, 2008, **36**, 253-387.
61. A. J. Jacobson, J. T. Lewandowski and J. W. Johnson, *Journal of The Less-Common Metals*, 1986, **116**, 137-146.

62. R. Schaak and T. Mallouk, *Chemistry of Materials*, 2002, **14**, 1455-1471.
63. C. Sun, P. Peng, L. Zhu, W. Zheng and Y. Zhao, *European Journal of Inorganic Chemistry*, 2008, **2008**, 3864-3870.
64. S. Uma, A. R. Raju and J. Gopalakrishnan, *Journal of Materials Chemistry*, 1993, **3**, 709-713.
65. Y. Bréard, C. Michel, M. Hervieu, N. Nguyen, A. Ducouret, V. Hardy, A. Maignan, B. Raveau, F. Bourée and G. André, *Chemistry of Materials*, 2004, **16**, 2895-2905.
66. A. Demont, D. Pelloquin, S. Hébert, Y. Bréard, J. Höwing, Y. Miyazaki and A. Maignan, *Journal of Solid State Chemistry*, 2011, **184**, 1655-1660.
67. K.-A. Hyeon and S.-H. Byeon, *Chemistry of Materials*, 1998, **11**, 352-357.
68. L. Yan, H. Niu, C. A. Bridges, P. A. Marshall, J. Hadermann, G. van Tendeloo, P. R. Chalker and M. J. Rosseinsky, *Angewandte Chemie International Edition*, 2007, **46**, 4539-4542.
69. L. Yan, H. J. Niu, G. V. Duong, M. R. Suchomel, J. Bacsa, P. R. Chalker, J. Hadermann, G. van Tendeloo and M. J. Rosseinsky, *Chemical Science*, 2011, **2**, 261-272.
70. M. Nanot, F. Queyroux and J.-C. Gilles, *Journal of Solid State Chemistry*, 1979, **28**, 137-147.
71. M. Nanot, F. Queyroux, J.-C. Gilles, A. Carpy and J. Galy, *Journal of Solid State Chemistry*, 1974, **11**, 272-284.
72. R. Portier, M. Fayard, A. Carpy and J. Galy, *Materials Research Bulletin*, 1974, **9**, 371-377.
73. R. Portier, A. Carpy, M. Fayard and J. Galy, *Physica Status Solidi (a)*, 1975, **30**, 683-697.
74. F. Lichtenberg, A. Herrnberger, K. Wiedenmann and J. Mannhart, *Progress in Solid State Chemistry*, 2001, **29**, 1-70.
75. J. G. Bednorz and K. A. Müller, *Zeitschrift für Physik B Condensed Matter*, 1986, **64**, 189-193.
76. M. K. Wu, J. R. Ashburn, C. J. Torng, P. H. Hor, R. L. Meng, L. Gao, Z. J. Huang, Y. Q. Wang and C. W. Chu, *Physical Review Letters*, 1987, **58**, 908-910.
77. Y. LePage, W. R. McKinnon, J. M. Tarascon, L. H. Greene, G. W. Hull, Hwang and M. D, *Physical Review B*, 1987, **35**, 7245-7248.
78. H. Shaked, *Crystal structures of the high-Tc superconducting copper-oxides*, Elsevier Science Publishers B.V., 1994.
79. P. Woodward, *Acta Crystallographica Section B*, 1997, **53**, 32-43.
80. P. Woodward, *Acta Crystallographica Section B*, 1997, **53**, 44-66.
81. K. S. Aleksandrov and J. Bartolomé, *Phase Transitions*, 2001, **74**, 255-335.
82. M. Nanot, F. Queyroux, J.-C. Gilles and R. Chevalier, *Acta Crystallographica Section B*, 1976, **32**, 1115-1120.
83. D. M. Ogborne and M. T. Weller, *Physica C: Superconductivity*, 1994, **230**, 153-158.
84. C. Chaillout, S. W. Cheong, Z. Fisk, M. S. Lehmann, M. Marezio, B. Morosin and J. E. Schirber, *Physica C: Superconductivity*, 1989, **158**, 183-191.
85. Y. Le Page, T. Siegrist, S. A. Sunshine, L. F. Schneemeyer, D. W. Murphy, S. M. Zahurak, J. V. Waszczak, W. R. McKinnon, J. M. Tarascon, G. W. Hull and L. H. Greene, *Physical Review B*, 1987, **36**, 3617-3621.
86. C. Tenailleau, M. Allix, J. Claridge, M. Hervieu, M. Thomas, J. Hirst and M. Rosseinsky, *Journal of the American Chemical Society*, 2008, **130**, 7570-7583.
87. A. Demont, M. S. Dyer, R. Sayers, M. F. Thomas, M. Tsiamtsouri, H. N. Niu, G. R. Darling, A. Daoud-Aladine, J. B. Claridge and M. J. Rosseinsky, *Chemistry of Materials*, 2010, **22**, 6598-6615.

88. D. B. Mitzi, in *Progress in Inorganic Chemistry*, John Wiley & Sons, Inc., 2007, pp. 1-121.
89. F. Gäbler, Y. Prots and R. Niewa, *Zeitschrift für anorganische und allgemeine Chemie*, 2007, **633**, 93-97.
90. F. Gäbler, D. Bräunling, W. Schnelle, I. Schellenberg, R. Pöttgen and R. Niewa, *Zeitschrift für anorganische und allgemeine Chemie*, 2011, **637**, 977-982.
91. D. B. Mitzi, C. A. Feild, W. T. A. Harrison and A. M. Guloy, *Nature*, 1994, **369**, 467-469.
92. D. B. Mitzi, S. Wang, C. A. Feild, C. A. Chess and A. M. Guloy, *Science*, 1995, **267**, 1473-1476.
93. J. M. Perez-Mato, M. Zakhour-Nakhl, F. Weill and J. Darriet, *Journal of Materials Chemistry*, 1999, **9**, 2795-2807.
94. Y. Takeda, F. Kanamura, M. Shimada and M. Koizumi, *Acta Crystallographica Section B*, 1976, **32**, 2464-2466.
95. W. Wong-Ng, J. A. Kaduk, R. A. Young, F. Jiang, L. J. Swartzendruber and H. J. Brown, *Powder Diffraction*, 1999, **14**, 181-189.
96. S. Wang, D. B. Mitzi, C. A. Feild and A. Guloy, *Journal of the American Chemical Society*, 1995, **117**, 5297-5302.
97. N. Barrier, D. Pelloquin, N. Nguyen, M. Giot, F. Bourée and B. Raveau, *Chemistry of Materials*, 2005, **17**, 6619-6623.
98. M. A. Peña and J. L. G. Fierro, *Chemical Reviews*, 2001, **101**, 1981-2018.
99. H. Tanaka, *Catalysis Surveys from Asia*, 2005, **9**, 63-74.
100. L. J. Tejuca, *Properties and Applications of Perovskite-type Oxides*, 1993.
101. L. G. Tejuca, J. L. G. Fierro and J. M. D. Tascón, in *Advances in Catalysis*, eds. H. P. D.D. Eley and B. W. Paul, Academic Press, 1989, vol. Volume 36, pp. 237-328.
102. R. J. H. Voorhoeve, D. W. Johnson Jr, J. P. Remeika and P. K. Gallagher, *Science*, 1977, **195**, 827-833.
103. M. A. Gómez-García, V. Pitchon and A. Kiennemann, *Environment International*, 2005, **31**, 445-467.
104. J. M. D. Tascón, L. G. Tejuca and C. H. Rochester, *Journal of Catalysis*, 1985, **95**, 558-566.
105. S. Takashi, *Applied Catalysis*, 1986, **28**, 81-88.
106. D. Ferri and L. Forni, *Applied Catalysis B: Environmental*, 1998, **16**, 119-126.
107. R. J. H. Voorhoeve, J. P. Remeika and L. E. Trimble, *Annals of the New York Academy of Sciences*, 1976, **272**, 3-21.
108. M. Machida, H. Murakami and T. Kijima, *Applied Catalysis B: Environmental*, 1998, **17**, 195-203.
109. M. Machida, H. Murakami, T. Kitsubayashi and T. Kijima, *Chemistry of Materials*, 1997, **9**, 135-140.
110. J. Duffy, *Geochim. Cosmochim. Acta*, 1993, **57**, 3961-3970.
111. J. Duffy and M. Ingram, *J. Am. Chem. Soc.*, 1971, **93**, 6448-6454.
112. J. A. Duffy, *J. Phys. Chem. B*, 2004, **108**, 14137-14141.
113. E. Bordes-Richard, *Topics in Catalysis*, 2008, **50**, 82-89.
114. Moriceau P., Lebouteiller A., Bordes E. and C. P., *Phys. Chem. Chem. Phys.*, 1999, **1**, 5734.
115. J. E. ten Elshof, H. J. M. Bouwmeester and H. Verweij, *Applied Catalysis A: General*, 1995, **130**, 195-212.
116. F. Mudu, B. Arstad, E. Bakken, H. Fjellvåg and U. Olsbye, *Journal of Catalysis*, 2010, **275**, 25-33.
117. V. Knox, *American Ceramic Society Bulletin*, 2010, **89**, 31.

118. K. Maeda and T. E. Mallouk, *Journal of Materials Chemistry*, 2009, **19**, 4813-4818.
119. J. W. Fergus, *Sensors and Actuators B: Chemical*, 2007, **123**, 1169-1179.
120. J. C. Boivin and G. Mairesse, *Chemistry of Materials*, 1998, **10**, 2870-2888.
121. K. R. Kendall, C. Navas, J. K. Thomas and H.-C. z. Loye, *Solid State Ionics*, 1995, **82**, 215-223.
122. K. D. Kreuer, *Ann. Rev. Mater. Res.*, 2003, **33**, 333-359.
123. T. Norby, *Journal of Materials Chemistry*, 2001, **11**, 11-18.
124. B. Rapp, *Materials Today*, 2003, **6**, 13.
125. Y. Inaguma, C. Liquan, M. Itoh, T. Nakamura, T. Uchida, H. Ikuta and M. Wakihara, *Solid State Communications*, 1993, **86**, 689-693.
126. L. Malavasi, C. A. J. Fisher and M. S. Islam, *Chemical Society Reviews*, 2010, **39**, 4370-4387.
127. S. Stramare, V. Thangadurai and W. Weppner, *Chemistry of Materials*, 2003, **15**, 3974-3990.
128. A. Manthiram, F. Prado and T. Armstrong, *Solid State Ionics*, 2002, **152-153**, 647-655.
129. T. Norby, *Journal of Chemical Engineering of Japan*, 2007, **40**, 1166-1171.
130. S. Skinner, *Int J Inorg Mater*, 2001, **3**, 113-121.
131. Q. X. Fu and F. Tietz, *Fuel Cells*, 2008, **8**, 283-293.
132. V. V. Kharton, F. M. B. Marques and A. Atkinson, *Solid State Ionics*, 2004, **174**, 135-149.
133. M. V. Patrakeev, I. A. Leonidov, V. L. Kozhevnikov and V. V. Kharton, *Solid State Sciences*, 2004, **6**, 907-913.
134. E. Tsipis and V. Kharton, *Journal of Solid State Electrochemistry*, 2011, **15**, 1007-1040.
135. D. Rembelski, J. P. Viricelle, L. Combemale and M. Rieu, *Fuel Cells*, 2012, n/a-n/a.
136. K. Yashiro, S. Akoshima, T. Kudo, M. Oishi, H. Matsumoto, K. Sato, T. Kawada and J. Mizusaki, *Solid State Ionics*, 2011, **192**, 76-82.
137. N. Ito, M. Iijima, K. Kimura and S. Iguchi, *Journal of Power Sources*, 2005, **152**, 200-203.
138. T. J. Seebeck, *Abhandlungen der Königlichen Preußischen Akademie der Wissenschaften zu Berlin* 1823, 265.
139. T. M. Tritt and M. A. Subramanian, *MRS Bulletin*, 2006, **31**, 188-198.
140. K. Koumoto, I. Terasaki and R. Funahashi, *MRS Bulletin*, 2006, **31**, 206-210.
141. R. Funahashi, A. Kosuga, N. Miyasou, E. Takeuchi, S. Urata, K. Lee, H. Ohta and K. Koumoto, 2007.
142. R. Robert, L. Bocher, B. Sipos, M. Döbeli and A. Weidenkaff, *Progress in Solid State Chemistry*, 2007, **35**, 447-455.
143. R. Ang, Y. P. Sun and W. H. Song, *Journal of Physics D: Applied Physics*, 2007, **40**, 5206.
144. S. G. Ebbinghaus, H.-P. Abicht, R. Dronskowski, T. Müller, A. Reller and A. Weidenkaff, *Progress in Solid State Chemistry*, 2009, **37**, 173-205.
145. N. F. Mott, *Metal-Insulator Transitions*, Taylor & Francis, London, 1990.
146. J. B. Goodenough, *Physical Review*, 1960, **117**, 1442-1451.
147. J. B. Goodenough, *Physical Review*, 1955, **100**, 564-573.
148. J. Goodenough, *Czechoslovak Journal of Physics*, 1967, **B 17** 304-366.
149. J. Kanamori, *Journal of Physics and Chemistry of Solids*, 1959, **10**, 87-98.
150. A. L. Efros and B. I. Shklovskii, *Journal of Physics C: Solid State Physics*, 1975, **8**, L49.
151. J. Zaanen, G. A. Sawatzky and J. W. Allen, *Physical Review Letters*, 1985, **55**, 418.

152. Y. V. Kolen'ko, K. A. Kovnir, I. S. Neira, T. Taniguchi, T. Ishigaki, T. Watanabe, N. Sakamoto and M. Yoshimura, *The Journal of Physical Chemistry C*, 2007, **111**, 7306-7318.
153. M. Alexe, C. Harnagea, A. Visinoiu, A. Pignolet, D. Hesse and U. Gösele, *Scripta Materialia*, 2001, **44**, 1175-1179.
154. J. F. Scott, *Science*, 2007, **315**, 954-959.
155. L. E. Cross, *Materials Chemistry and Physics*, 1996, **43**, 108-115.
156. J. Scott, eds. N. Dalal and A. Bussmann-Holder, Springer Berlin / Heidelberg, 2007, vol. 124, pp. 199-207.
157. E. Sawaguchi, *Ferroelectrics*, 2002, **266**, 341-353.
158. A. P. Ramirez, M. A. Subramanian, M. Gardel, G. Blumberg, D. Li, T. Vogt and S. M. Shapiro, *Solid State Communications*, 2000, **115**, 217-220.
159. H. Nagata, N. Koizumi, N. Kuroda, I. Igarashi and T. Takenaka, *Ferroelectrics*, 1999, **229**, 273-278.
160. G. Catalan, *Phase Transitions*, 2008, **81**, 729-749.
161. M. Imada, A. Fujimori and Y. Tokura, *Reviews of Modern Physics*, 1998, **70**, 1039.
162. A. R. West, *Basic solid state chemistry*, Wiley, Chichester, 1999.
163. T. Takeda and H. Watanabe, *Journal of the Physical Society of Japan*, 1972, **33**, 973.
164. C. Autret, C. Martin, M. Hervieu, A. Maignan, B. Raveau, G. André, F. Bourée and Z. Jirak, *Journal of Magnetism and Magnetic Materials*, 2004, **270**, 194-202.
165. J. Blasco, J. Stankiewicz and J. García, *Journal of Solid State Chemistry*, 2006, **179**, 898-908.
166. S. Kawasaki, M. Takano and Y. Takeda, *Solid State Ionics*, 1998, **108**, 221-226.
167. S. Chakraverty, A. Ohtomo, D. Okuyama, M. Saito, M. Okude, R. Kumai, T. Arima, Y. Tokura, S. Tsukimoto, Y. Ikuhara and M. Kawasaki, *Physical Review B*, 2011, **84**, 064436.
168. D. D. Khalyavin, L. C. Chapon, E. Suard, J. E. Parker, S. P. Thompson, A. A. Yaremchenko and V. V. Kharton, *Physical Review B*, 2011, **83**, 140403.
169. P. Adler, *Journal of Solid State Chemistry*, 1997, **130**, 129-139.
170. E. Iguchi, K. Ueda and H. Nakatsugawa, *Journal of Physics: Condensed Matter*, 1998, **10**, 8999.
171. T. Motohashi, B. Raveau, M. Hervieu, A. Maignan, V. Pralong, N. Nguyen and V. Caignaert, *Journal of Physics: Condensed Matter*, 2006, **18**, 2157-2171.
172. A. P. Ramirez, *Journal of Physics Condensed Matter*, 1997, **9**, 8171-8199.
173. K. I. Kobayashi, T. Kimura, H. Sawada, K. Terakura and Y. Tokura, *Nature*, 1998, **395**, 677-680.
174. G. Lawes and G. Srinivasan, *Journal of Physics D: Applied Physics*, 2011, **44**, 243001.
175. K. Terakura, *Progress in Materials Science*, 2007, **52**, 388-400.
176. M. Bibes and A. Barthelemy, *Electron Devices, IEEE Transactions on*, 2007, **54**, 1003-1023.
177. M. Bibes, J. E. Villegas and A. Barthélémy, *Advances In Physics*, 2011, **60**, 5-84.
178. P. Grünberg, R. Schreiber, Y. Pang, M. B. Brodsky and H. Sowers, *Physical Review Letters*, 1986, **57**, 2442-2445.
179. M. N. Baibich, J. M. Broto, A. Fert, F. N. Van Dau, F. Petroff, P. Etienne, G. Creuzet, A. Friederich and J. Chazelas, *Physical Review Letters*, 1988, **61**, 2472-2475.
180. M. Julliere, *Physics Letters A*, 1975, **54**, 225-226.
181. L. Alff, eds. K. Scharnberg and S. Kruchinin, Springer Netherlands, 2007, vol. 241, pp. 393-400.
182. G. H. Jonker and J. H. Van Santen, *Physica*, 1950, **16**, 337-349.
183. J. H. Van Santen and G. H. Jonker, *Physica*, 1950, **16**, 599-600.

184. J. Fontcuberta, L. Balcells, M. Bibes, J. Navarro, C. Frontera, J. Santiso, J. Fraxedas, B. Martínez, S. Nadolski, M. Wojcik, E. Jedryka and M. J. Casanove, *Journal of Magnetism and Magnetic Materials*, 2002, **242–245, Part 1**, 98-104.
185. M. Bibes and A. Barthelemy, *Nat Mater*, 2008, **7**, 425-426.
186. R. Hott, R. Kleiner, T. Wolf and G. Zwicknagl, ed. A. V. Narlikar, Springer Berlin Heidelberg, 2005, pp. 1-69.
187. Y. Maeno, H. Hashimoto, K. Yoshida, S. Nishizaki, T. Fujita, J. G. Bednorz and F. Lichtenberg, *Nature*, 1994, **372**, 532-534.
188. Y. Mizuguchi and Y. Takano, *Journal of the Physical Society of Japan*, 2010, **79**, 102001-102019.
189. M. R. Norman, *Physics*, 2008, **1**, 21.
190. M. Kakihana, *Journal of Sol-Gel Science and Technology*, 1996, **6**, 7-55.
191. P. Karen, *Journal of Solid State Chemistry*, 2006, **179**, 3167-3183.
192. L. Jantsky, H. Okamoto, M. F. Thomas, P. Karen, M. J. Rosseinsky and H. Fjellvåg, *to be published*.
193. B. C. Hauback, H. Fjellvåg, O. Steinsvoll, K. Johansson, O. T. Buset and J. Jørgensen, *Journal of Neutron Research*, 2000, **8**, 215-232.
194. P. W. Atkins and D. F. Shriver, *Inorganic chemistry*, 5th Edition edn., Oxford University Press, Oxford, 2009.
195. P. Gütlich, *Lecture Notes "Mössbauer Spectroscopy"*,2005, http://www.ak-guetlich.chemie.uni-mainz.de/Dateien/Moessbauer_Lectures.pdf.
196. K. Kuzushita, S. Morimoto, S. Nasu, S. Kawasaki and M. Takano, *Hyperfine Interactions*, 2002, **141-142**, 199-205.
197. K. Kuzushita, S. Morimoto, S. Nasu, S. Kawasaki and M. Takano, *Solid State Communications*, 2002, **123**, 107-111.
198. T. Armstrong, F. Prado and A. Manthiram, *Solid State Ionics*, 2001, **140**, 89-96.
199. F. Prado, K. Gurunathan and A. Manthiram, *Journal of Materials Chemistry*, 2002, **12**, 2390-2395.
200. J. Y. Lee, J. S. Swinnea, H. Steinfink, W. M. Reiff, S. Pei and J. D. Jorgensen, *Journal of Solid State Chemistry*, 1993, **103**, 1-15.
201. K. Lee and A. Manthiram, *Chemistry of Materials*, 2006, **18**, 1621-1626.
202. A. Olafsen, H. Fjellvag and B. C. Hauback, *Journal of Solid State Chemistry*, 2000, **151**, 46-55.
203. Z. Zhang and M. Greenblatt, *Journal of Solid State Chemistry*, 1995, **117**, 236-246.
204. R. Shannon, *Acta Crystallographica Section A*, 1976, **32**, 751-767.
205. M. Burriel, G. Garcia, M. D. Rossell, A. Figueras, G. Van Tendeloo and J. Santiso, *Chemistry of Materials*, 2007, **19**, 4056-4062.
206. L. Jantsky, P. Norby, M. J. Rosseinsky and H. Fjellvåg, *Zeitschrift für Kristallographie*, 2009, **224**, 295-301.
207. S. Nishimoto, M. Matsuda, S. Harjo, A. Hoshikawa, T. Ishigaki, T. Kamiyama and M. Miyake, *Journal of Solid State Chemistry*, 2006, **179**, 3308-3313.
208. M. Lehtimaki, A. Hirasa, M. Matvejeff, H. Yamauchi and M. Karppinen, *Journal of Solid State Chemistry*, 2007, **180**, 3247-3252.
209. M. Matvejeff, M. Lehtimaki, A. Hirasa, Y. H. Huang, H. Yamauchi and M. Karppinen, *Chemistry of Materials*, 2005, **17**, 2775-2779.
210. S. E. Dann, M. T. Weller, D. B. Currie, M. F. Thomas and A. D. Alrawwas, *Journal of Materials Chemistry*, 1993, **3**, 1231-1237.
211. P. Adler, A. Goncharov and K. Syassen, *Hyperfine Interactions*, 1995.
212. P. D. Battle, T. C. Gibb and S. Nixon, *Journal of Solid State Chemistry*, 1988, **77**, 124-131.

213. P. Adler and S. Ghosh, *Solid State Sciences*, 2003, **5**.
214. S. Ghosh and P. Adler, *Solid State Commun*, 2000.
215. R. S. Perry, L. M. Galvin, S. A. Grigera, L. Capogna, A. J. Schofield, A. P. Mackenzie, M. Chiao, S. R. Julian, S. I. Ikeda, S. Nakatsuji, Y. Maeno and C. Pfleiderer, *Physical Review Letters*, 2001, **86**, 2661-2664.
216. P. Ravindran, H. Fjellvag, A. Kjekshus, P. Blaha, K. Schwarz and J. Luitz, *Journal of Applied Physics*, 2002, **91**, 291-303.
217. J. B. Goodenough, R. I. Dass and J. Zhou, *Solid State Sciences*, 2002, **4**, 297-304.
218. H. D. Zhou and J. B. Goodenough, *Journal of Solid State Chemistry*, 2004, **177**, 3339-3345.
219. M. Sánchez-Andújar, J. Mira, J. Rivas and M. A. Senaris-Rodriguez, *Journal of Magnetism and Magnetic Materials*, 2003, **263**, 282-288.
220. D. Akahoshi, J.-i. Tozawa, R. Nakamura, M. Akaki and H. Kuwahara, *Journal of the Physical Society of Japan*, 2011, **80**, 124702.
221. E. V. Tsipis, E. N. Naumovich, M. V. Patrakeev, P. V. Anikina, J. o. C. Waerenborgh and V. V. Kharton, *Chemistry of Materials*, 2009, **21**, 5072-5078.
222. A. Ohtomo and H. Y. Hwang, *Nature*, 2004, **427**, 423-426.

Apendix

I

II

III